Supplementary Information

Gallium-based intermetallic compounds with tailored active site configurations for electrochemical ammonia synthesis

Huaifang Zhang[1,2,6], Chaoqun Ma[1,2,6], Yi-Chi Wang[3,6], Xiaojuan Zhu[4], Kaiyu Qu[4], Caihong He[1,2], Sumei Han[1,2], Ai-Hua Liu[1,2], Qi Wang[1], Wenbin Cao[1], Lijie Zhu[5], Lin Gu[3], An-Liang Wang[4*], Qipeng Lu[1,2*]

[1]School of Materials Science and Engineering, University of Science and Technology Beijing, Beijing 100083, China.
[2]Shunde Innovation School, University of Science and Technology Beijing, Foshan 528399, China.
[3]Beijing National Center for Electron Microscopy and Laboratory of Advanced Materials, School of Materials Science and Engineering, Tsinghua University, Beijing 100084, China.
[4]School of Chemistry and Chemical Engineering, Shandong University, Jinan 250100, China.
[5]School of Instrument Science and Opto-Electronics Engineering, Beijing Information Science and Technology University, Beijing 100192, China.

[6]These authors contributed equally: Huaifang Zhang, Chaoqun Ma, Yi-Chi Wang

*Corresponding author.
E-mail: qipeng@ustb.edu.cn (Q.L.) and alwang@sdu.edu.cn (A.-L.W.).

Table of Contents

Methods 3
Chemicals and reagents 3
Synthesis of CoGa/NG 4
Synthesis of Co/NG 4
Synthesis of pure NG 4
Physicochemical characterizations 4
Electrochemical measurements 6
Determination of NH_4^+-N concentration 6
Determination of NO_3^--N concentration 7
Determination of NO_2^--N concentration 7
Determination of N_2H_4-N concentration 7
Determination of NH_3 yield, NH_3 FE, and NH_3 selectivity 8
^{15}N isotope labeling and ^1H NMR experiments 9
Electrochemical *in-situ* ATR-FTIR experiments 9
Online differential electrochemical mass spectrometry (DEMS) measurements 10
Calculation details 10
Assembly of Zn-NO_3^- battery 11
Supplementary Figures 12
Supplementary Tables 58
Supplementary References 64

Methods

Chemicals and reagents. Gallium nitrate hydrate ($Ga(NO_3)_3 \cdot xH_2O$, 99.99%), rhodium nitrate solution ($Rh(NO_3)_3$) in dilute nitric acid solution with 10 wt% of Rh, potassium hydroxide (KOH, 90%) sodium nitrate-^{15}N ($Na^{15}NO_3$, 98.5%), ammonium chloride-^{15}N ($^{15}NH_4Cl$, 98.5%), salicylic acid ($C_7H_6O_3$, 99.5%), sodium citrate dihydrate ($C_6H_5Na_3O_7 \cdot 2H_2O$, 99.0%), sodium hypochlorite solution (NaClO, available chlorine 5.5~6.5%), sodium nitroferricyanide(III) dihydrate ($Na_2[Fe(CN)_5(NO)] \cdot 2H_2O$, 99.0%), p-dimethylaminobenzaldehyde ($C_9H_{11}NO$), N-(1-Naphthyl)ethylenediamine dihydrochloride ($C_{12}H_{14}N_2 \cdot 2HCl$, 98%), sulfanilamide ($C_6H_8N_2O_2S$, 99.5%), deuterium oxide (D_2O, 99.9 atom% D), and maleic acid ($C_4H_4O_4$, 99.0%) were afforded by Macklin Biochemical Co., Ltd (Shanghai, China). Graphene oxide (GO) was supplied from Nanjing XFNANO Materials Tech Co., Ltd (Nanjing, China). Cobalt nitrate hexahydrate ($Co(NO_3)_2 \cdot 6H_2O$, 98.5%), nickel nitrate hexahydrate ($Ni(NO_3)_2 \cdot 6H_2O$, 98.0%), sodium nitrate-^{14}N ($Na^{14}NO_3$, 99.0%), sodium nitrite ($NaNO_2$, 99.0%), sodium hydroxide (NaOH, 96.0%), hydrazine hydrate aqueous solution ($N_2H_4 \cdot xH_2O$), ammonium chloride-^{14}N ($^{14}NH_4Cl$, 99.5%), hydrochloric acid (HCl), phosphoric acid (H_3PO_4), and poly (vinyl alcohol) (PVA, $Mw = 1750 \pm 50$) were purchased from Sinopharm Chemical Reagent Co., Ltd (Shanghai, China). Potassium tetrachloroplatinate (K_2PtCl_4, 98%) and potassium tetrachloropalladate (K_2PdCl_4, 98%) were obtained from Aladdin Biochemical Technology Co., Ltd (Shanghai, China). All reagents and chemicals were used without further purification.

Synthesis of CoGa/NG. In the standard procedure, 0.075 mmol of $Co(NO_3)_2 \cdot 6H_2O$ and 0.075 mmol of $Ga(NO_3)_3 \cdot 9H_2O$ were completely dispersed in 0.5 mL of PVA aqueous solution (20 mg mL^{-1}). Subsequently, 4 mL of GO aqueous solution (16 mg mL^{-1}) was rapidly added into the aforementioned PVA solution with vigorous shaking at room temperature, resulting in the formation of $Co(NO_3)_2$-$Ga(NO_3)_3$/GO-PVA hydrogels. Next, the obtained hydrogels were freeze-dried at -50 °C for 24 hours to form the $Co(NO_3)_2$-$Ga(NO_3)_3$/GO-PVA aerogels. Finally, the aerogels were annealed at a temperature of 900 °C for 6 hours under a mixed atmosphere of H_2/Ar (containing 10 vol.% H_2) with a heating rate of 5 °C min^{-1} to obtain CoGa/NG aerogels. The resulting products were washed several times with deionized water. Furthermore, a wide range of Ga-based intermetallic compounds, including $Ni_{13}Ga_9$, $Ni_{1.91}Ga$, Ni_3Ga, PtGa, Pt_5Ga_3, Pt_3Ga, Pd_5Ga_3, Pd_2Ga, RhGa, and various others, were synthesized employing similar processes except for replacing the metal precursor salts.

Synthesis of Co/NG. The synthesis process for Co/NG was similar to those of CoGa/NG, excluding the addition of $Ga(NO_3)_3 \cdot 9H_2O$.

Synthesis of pure NG. The synthesis process for pure NG was similar to those of CoGa/NG, excluding the simultaneous addition of $Co(NO_3)_2 \cdot 6H_2O$ and $Ga(NO_3)_3 \cdot 9H_2O$. Instead, $NaNO_3$ was used as the nitrogen source in the synthesis of pure NG.

Physicochemical characterizations. The crystal structure of the prepared samples was investigated by X-ray powder diffraction (XRD) using a Bruker D8 Advance

diffractometer with Cu Kα radiation (λ = 1.54 Å). The morphology and microstructure of the nanomaterials were characterized by scanning electron microscopy (SEM, Hitachi S-4800), transmission electron microscopy (TEM, Hitachi HT7700), and high-resolution TEM (HRTEM, JEOL JEM-2100F). The high-angle annular dark-field scanning transmission electron microscopy (HAADF-STEM) images, aberration-corrected HAADF-STEM images, and energy-dispersive X-ray spectroscopy (EDX) elemental mapping images were taken using the transmission electron microscope (JEOL JEM-ARM300F Grand ARM) operated at 300 kV. X-ray photoelectron spectroscopy (XPS) measurements were performed on a Thermo Scientific ESCALAB 250Xi spectrometer with Al Kα as the excitation source (1486.6 eV), and all binding energies were calibrated according to the C 1s peak at 284.8 eV. N_2 adsorption-desorption measurements were carried out at 77 K using a Micromeritics ASAP-2460 Accelerated Surface Area and Porosimetry Analyzer. The specific surface area of the samples was estimated by the Brunauer-Emmett-Teller (BET) method. Raman spectra were acquired on a Horiba Jobin Yvon LabRam HR800 spectrometer using a 514 nm laser light. The metal contents of the electrocatalysts were accurately quantified by inductively coupled plasma atomic emission spectroscopy (ICP-AES) on an Agilent ICPOES730 instrument. The ultraviolet-visible (UV-Vis) absorption spectra were collected on a Shimadzu UV-1900 spectrophotometer. The ^{1}H nuclear magnetic resonance (NMR) spectra were performed on a Bruker Avance III HD 500 MHz spectrometer. The Co K-edge X-ray absorption spectroscopy (XAS) spectra were achieved at the BL14W1 station in Shanghai Synchrotron Radiation Facility (SSRF),

China.

Electrochemical measurements. All electrochemical measurements were performed on a CHI 760D electrochemical workstation (Shanghai, Chenhua Co.) adopting an H-type cell separated by a treated Nafion 211 membrane. The working electrode was prepared by dropping 0.1 mL of catalyst ink (5 mg mL^{-1}) onto carbon paper (CP, 1×1 cm^2). The counter electrode was a platinum foil, and the reference electrode was an Ag/AgCl electrode, respectively. All the potential values presented in this paper have been calibrated to the reversible hydrogen electrode (RHE) using the conversion formula: $E_{RHE} = E_{Ag/AgCl} + 0.0591\ pH + 0.197$. The linear sweep voltammetry (LSV) curves were recorded from 0.0 to -0.7 V with a sweep rate of 10 mV s^{-1} in 0.1 M KOH with and without 500 ppm NO_3^--N. The chronoamperometric curves were tested and maintained for one hour at different potentials.

Determination of NH_4^+-N concentration. The NH_4^+-N concentration was determined by the indophenol blue method. In detail, 2 mL of 1.0 M NaOH solution containing 5 wt% $C_7H_6O_3$ and 5 wt% $C_6H_5Na_3O_7 \cdot 2H_2O$, 1 mL of 0.05 M NaClO solution, and 0.2 mL of 1 wt% $Na_2[Fe(CN)_5(NO)] \cdot 2H_2O$ solution were added sequentially into 2 mL of diluted reaction solution (100 times dilution). The absorption intensity at a wavelength of 655 nm was recorded after coloring for 2 hours at room temperature. The standard curve was achieved by using a series of standard NH_4Cl solutions with known concentrations in 0.1 M KOH electrolyte. The fitting curve ($y = 0.489x + 0.028$, R^2=0.999) reveals a good linear relationship between the absorbance value and NH_4^+-

N concentration.

Determination of NO_3^--N concentration. After chronoamperometry tests, 2.6 mL of 0.05 M H_2SO_4 solution was added to 2 mL of diluted electrolyte (100 times dilution). The absorption intensities at wavelengths of 220 and 275 nm were recorded. The final absorbance values were calculated by the following equation ($A=A_{220nm}-2A_{275nm}$). The NO_3^--N concentration in the electrolyte was detected quantitatively based on the well-linearized calibration curve ($y = 0.111x + 0.004$, $R^2 = 0.999$), which was collected by measuring the absorption spectra of a series of standard $NaNO_3$ solutions with various concentrations in 0.1 M KOH electrolyte.

Determination of NO_2^--N concentration. The NO_2^--N concentration was detected through the Griess reagent. 0.1 g of $C_{12}H_{14}N_2 \cdot 2HCl$, 1.0 g of $C_6H_8N_2O_2S$, and 2.94 mL of H_3PO_4 were dissolved in 50 mL H_2O to obtain the Griess reagent. 1 mL of electrolyte was added to a beaker and then mixed with 2.0 mL of deionized water and 1.0 mL of color reagent in sequence. The absorption intensity at a wavelength of 540 nm was recorded after being maintained for 10 min at room temperature. The calibration curve ($y = 0.721x + 0.002$, $R^2=0.999$) was obtained by using a series of standard $NaNO_2$ solutions with different concentrations in 0.1 M KOH electrolyte, and a well-established linear relationship between absorbance value and NO_2^--N concentration was observed.

Determination of N_2H_4-N concentration. The presence of N_2H_4 in the electrolyte was assessed employing the Watt and Chrisp method. The coloring reagent was prepared by mixing 5.99 g of $C_9H_{11}NO$, 30 mL of concentrated HCl, and 300 mL of ethanol. 5 mL

of color reagent was added to 5 mL of electrolyte and then reacted for 10 min at room temperature. After that, the absorption intensity at a wavelength of 460 nm was recorded. The N_2H_4-N concentration in the electrolyte can be quantified according to the calibration curve ($y = 0.439x + 0.032$, $R^2=0.999$) plotted using a series of standard N_2H_4 solutions with a range of concentrations in 0.1 M KOH electrolyte.

Determination of NH_3 yield, NH_3 FE, and NH_3 selectivity

The NH_3 yield was calculated according to the following equation:

$$\mathrm{NH_3\ yield\ rate} = \frac{C_{\mathrm{NH3}} \times V}{t \times S}$$

where C_{NH3} is the produced NH_3 concentration, V is the electrolyte volume (25 mL), S is the geometric area of the working electrode (1 cm^2), and t is the reduction time (1 hour).

The NH_3 FE was calculated according to the following equation:

$$\mathrm{NH_3\ FE} = \frac{8F \times C_{\mathrm{NH3}} \times V}{M_{\mathrm{NH3}} \times Q} \times 100\%$$

where 8 is the number of electron transfers toward the formation of 1 mol of ammonia, F is the Faradaic constant (96485 C mol^{-1}), M_{NH3} is the molar mass of NH_3, and Q is the total charge passing through the electrode.

The NH_3 selectivity was calculated according to the following equation:

$$\mathrm{NH_3\ selectivity} = \frac{C}{C_0 - C_t} \times 100\%$$

where C is the concentration of produced NH_3, C_0 is the initial concentration of NO_3^-, and C_t is the concentration of NO_3^- after electrolysis.

^{15}N isotope labeling and ^{1}H NMR experiments. The NH_3 produced during the NO_3RR process was verified quantitatively by the isotope labeling experiment using $Na^{15}NO_3$ as the N source. After the electrolysis process, the electrolyte containing $^{15}NH_4^+$ was extracted and the pH value was adjusted to weak acidity by adding 0.05 M H_2SO_4 solution, and the NH_4^+ concentration was further determined by ^{1}H NMR (500 MHz) spectroscopy. The calibration curve was plotted as follows: Firstly, a series of standard $^{15}NH_4^+$ solutions having known concentrations in 0.1 M KOH electrolyte were prepared and adjusted to weak acidity by adding 0.05 M H_2SO_4. Secondly, 50 μL of deuterium oxide (D_2O) with maleic acid (4.4 mg/mL) was added to 0.5 mL of the above-mixed solution for the ^{1}H NMR detection. Finally, the calibration curve was achieved using the peak area ratio between $^{15}NH_4^+$ and maleic acid. The $^{15}NH_4^+$-^{15}N concentration in the electrolyte was estimated from the standard curve ($y = 0.008\ x + 0.053$, $R^2 = 0.999$) featuring a positive linear agreement between the peak area ratio value and $^{15}NH_4^+$-^{15}N concentration.

Electrochemical *in-situ* ATR-FTIR experiments. *In-situ* attenuated total reflection Fourier transform infrared (ATR-FTIR) spectra were conducted using a Thermo Scientific Nicolet 6700 spectrometer with a highly sensitive Mercury-Cadmium-Telluride (MCT) detector cooled with liquid nitrogen. The specially-made three-electrode thin-layer IR cell configuration utilizes CaF_2 as its optical window. In this device, the catalyst-dropped GCE, graphite rod, and Ag/AgCl electrode served as the working electrode, counter electrode, and reference electrode, respectively. *In-situ* ATR-IR spectra were recorded from 0.0 V to -0.7 V every 100 mV in 0.1 M KOH with

500 ppm NO_3^--N solution.

Online differential electrochemical mass spectrometry (DEMS) measurements. The DEMS tests were obtained on a QAS 100 device (Linglu Instruments, Shanghai). During the process, the electrolyte solution (0.1 M KOH + 500 ppm NO_3^--N) continuously flowed into a homemade electrochemical cell through a peristaltic pump. The catalyst-loaded glassy carbon electrode (GCE), platinum wire, and Ag/AgCl electrode were applied as the working electrode, counter electrode, and reference electrode, respectively. The chronoamperometric tests were performed at a fixed potential of -0.6 V when the baseline was stable. Then, the corresponding mass signals appeared. After completing the test and returning the mass signal to the baseline, the subsequent cycle commenced under identical conditions to minimize potential accidental errors during the DEMS measurements. The experiment concluded after five cycles.

Calculation details. All density functional theory (DFT) calculations were carried out using Vienna ab initio simulation package (VASP)[1, 2]. The generalized gradient approximation (GGA) with Perdew-Burke-Ernzerhof (PBE) functional was selected to accurately describe the exchange-correlation energy[3, 4]. The projector-augmented wave (PAW) pseudopotential was used to treat the interaction between the ionic cores and valence electrons[5]. The Van der Waals interactions were considered by the DFT-D3 method[6, 7]. The energy cutoff for the plane-wave basis was set as 500 eV. The Brillouin zone was sampled using a 3 × 3 × 1 Monkhorst-Pack k-point mesh. The convergence standards for the total energy and the Hellman-Feynman force were 10^{-5} eV and 0.05

eV $Å^{-1}$, respectively. A vacuum of 15 Å was added along the z-direction to avoid periodical interactions. To simulate the adsorption behavior of reaction intermediates on the catalyst surface, the CoGa (110) and Co (111) facets are chosen as the structural models for DFT calculations. The Gibbs free energy change (ΔG) of each elementary reaction can be computed by the following equation: $\Delta G = \Delta E + \Delta ZPE - T\Delta S$.

Where ΔE is the reaction energy difference, ΔZPE is the zero-point energy change, T is the temperature, and ΔS is the entropy change, respectively. The energy of the reaction can be calculated by the following reaction steps:

$$* + NO_3^- \rightarrow *NO_3 \quad (1)$$

$$*NO_3 + H^+ + e^- \rightarrow *NO_3H \quad (2)$$

$$*NO_3H + H^+ + e^- \rightarrow *NO_2 + H_2O \quad (3)$$

$$*NO_2 + H^+ + e^- \rightarrow *NO_2H \quad (4)$$

$$*NO_2H + H^+ + e^- \rightarrow *NO + H_2O \quad (5)$$

$$*NO + H^+ + e^- \rightarrow *NOH/^*NHO \quad (6)$$

$$*NOH + H^+ + e^- \rightarrow *NHOH \quad (7)$$

$$*NHOH + H^+ + e^- \rightarrow *NH_2OH \quad (8)$$

$$*NH_2OH + H^+ + e^- \rightarrow *NH_2 + H_2O \quad (9)$$

$$*NH_2 + H^+ + e^- \rightarrow *NH_3 \quad (10)$$

$$*NH_3 \rightarrow * + NH_3 \quad (11)$$

Assembly of Zn-NO_3^- battery. The as-prepared CoGa/NG (1×1 cm^2) and Zn plate (1×1 cm^2) were adopted as the cathode and anode of the Zn-NO_3^- battery, respectively. A typical H-type cell containing 25 mL of cathode electrolyte (1.0 M KOH + 0.1 M NO_3^-) and 25 mL of anode electrolyte (1.0 M KOH) was separated by a Nafion 211 membrane. All relevant battery data were recorded using a CHI 760D electrochemical workstation at room temperature.

Supplementary Figures

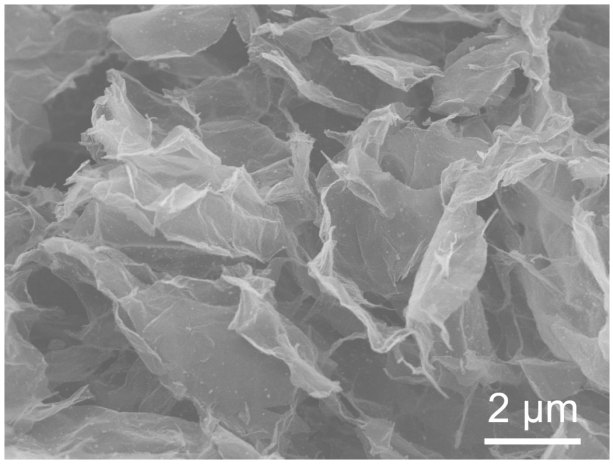

Supplementary Fig. 1 | SEM image of CoGa/NG. The sample presents an interconnected three-dimensional porous network structure.

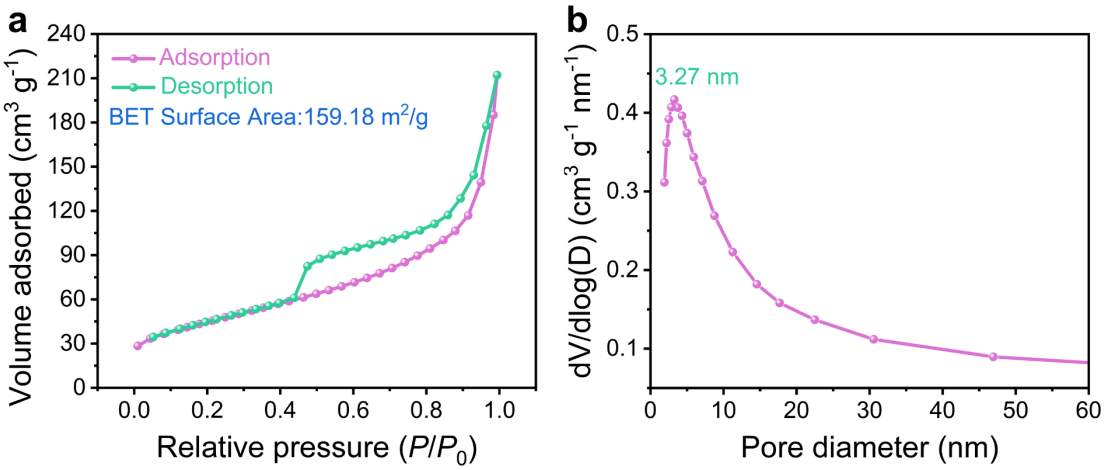

237

238 **Supplementary Fig. 2 | BET analysis of CoGa/NG. a** N_2 adsorption-desorption

239 isotherms. **b** The corresponding pore size distribution curve of CoGa/NG.

240

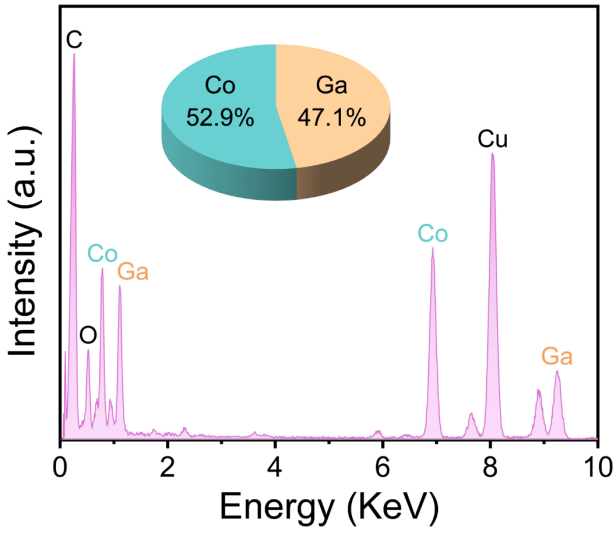

241

242 **Supplementary Fig. 3 | EDX spectrum of CoGa/NG.** The atomic ratio of Co to Ga is

243 determined to be 52.9:47.1.

244

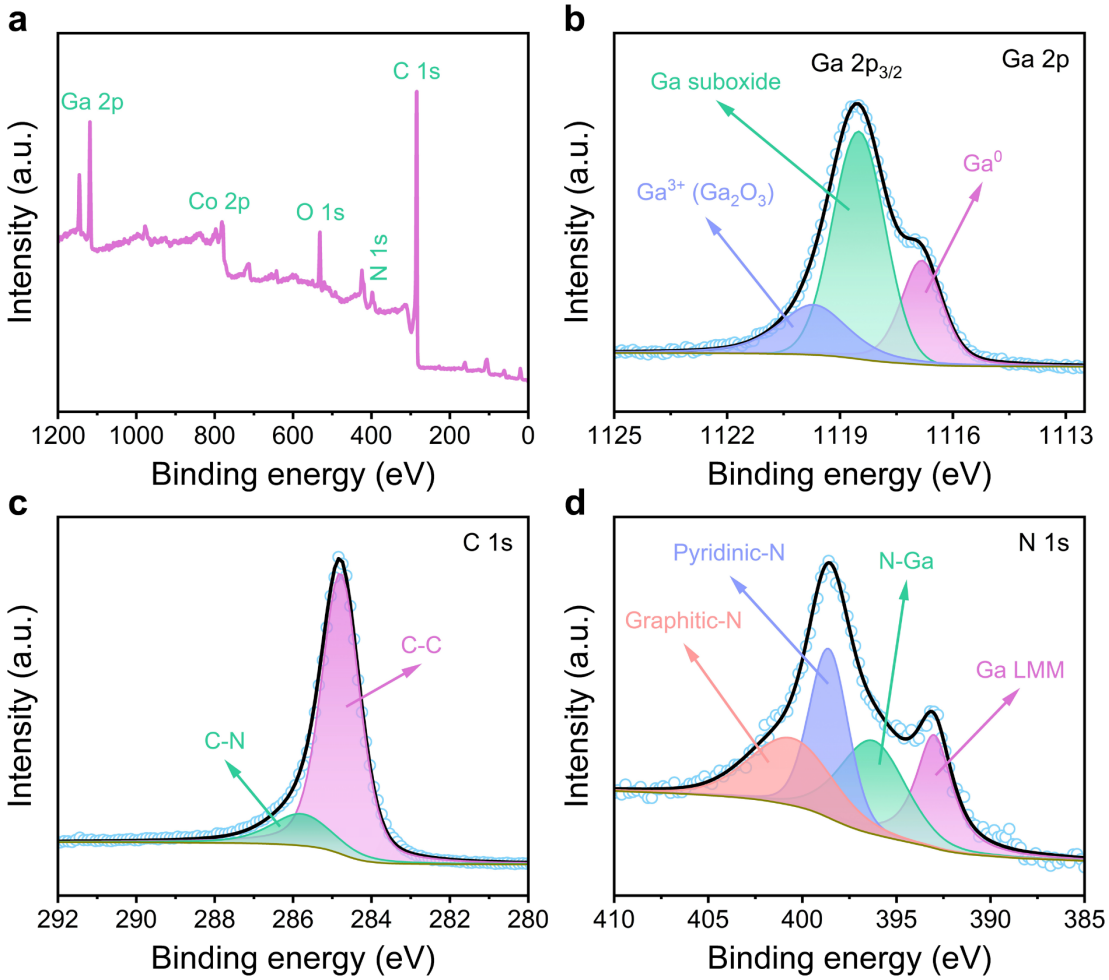

245

246 **Supplementary Fig. 4 | XPS analyses of CoGa/NG. a** XPS survey spectrum of

247 CoGa/NG. **b-d** High-resolution XPS spectra of CoGa/NG, Ga 2p (**b**), C 1s (**c**), and N

248 1s (**d**).

249

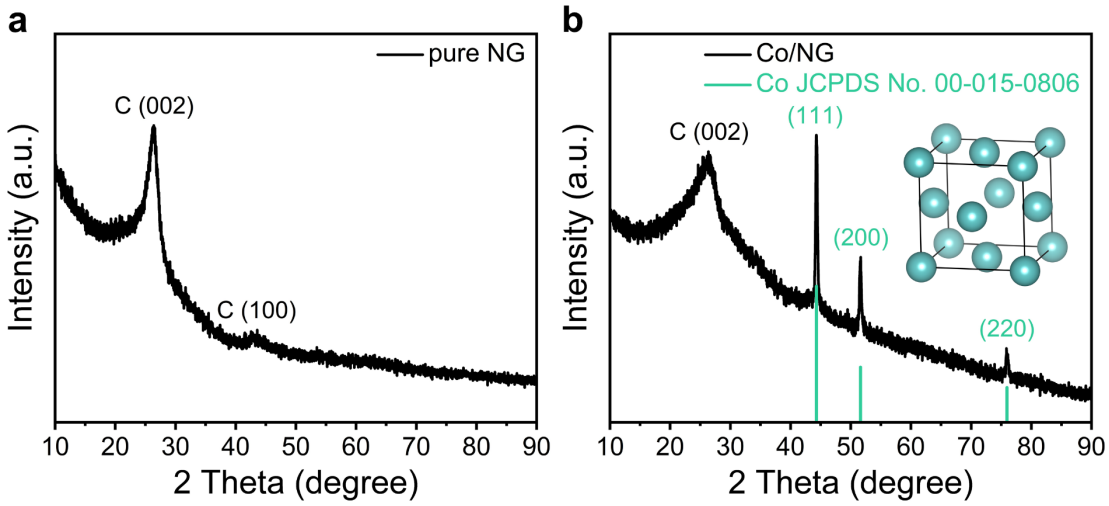

Supplementary Fig. 5 | XRD analyses. a, **b** XRD patterns of pure NG (**a**) and Co/NG (**b**).

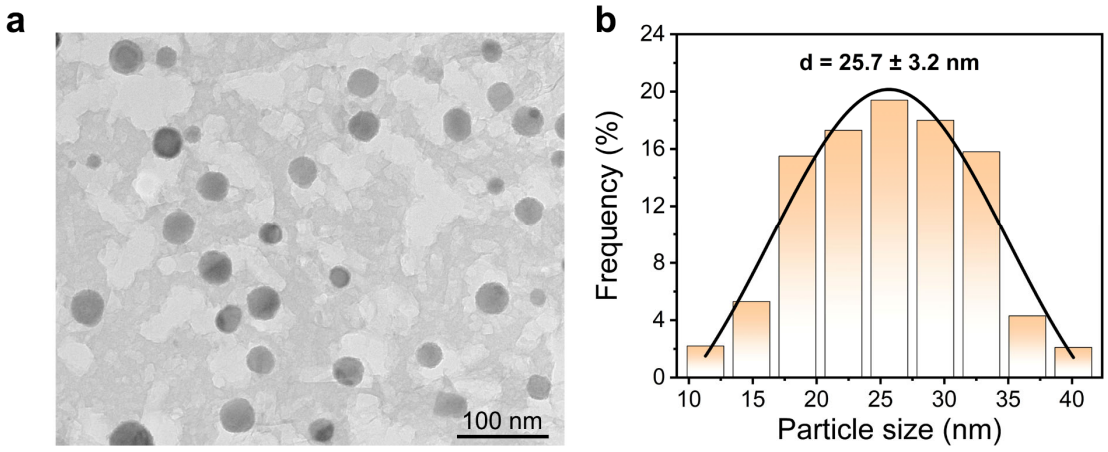

254

255 **Supplementary Fig. 6 | Measured average Co particle size in Co/NG. a** TEM image

256 of Co/NG. **b** The corresponding particle size distribution histogram.

257

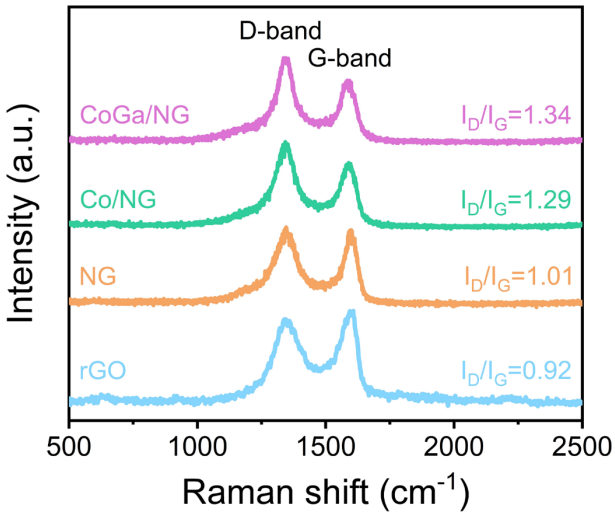

Supplementary Fig. 7 | Raman analyses. Raman spectra of rGO, NG, Co/NG, and CoGa/NG, where the G band (~1590 cm^{-1}) refers to sp^2-hybridized carbon and the D band (~1350 cm^{-1}) is related to the defects and disordered carbon.

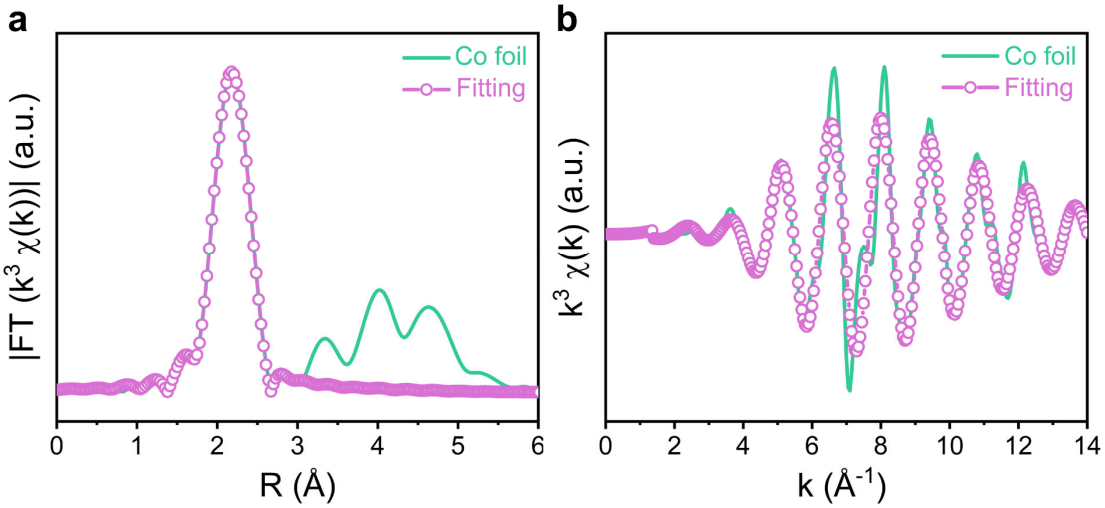

Supplementary Fig. 8 | The least-squares EXAFS fitting results. a, **b** EXAFS fitting curves of Co foil in R space (**a**) and k space (**b**), respectively.

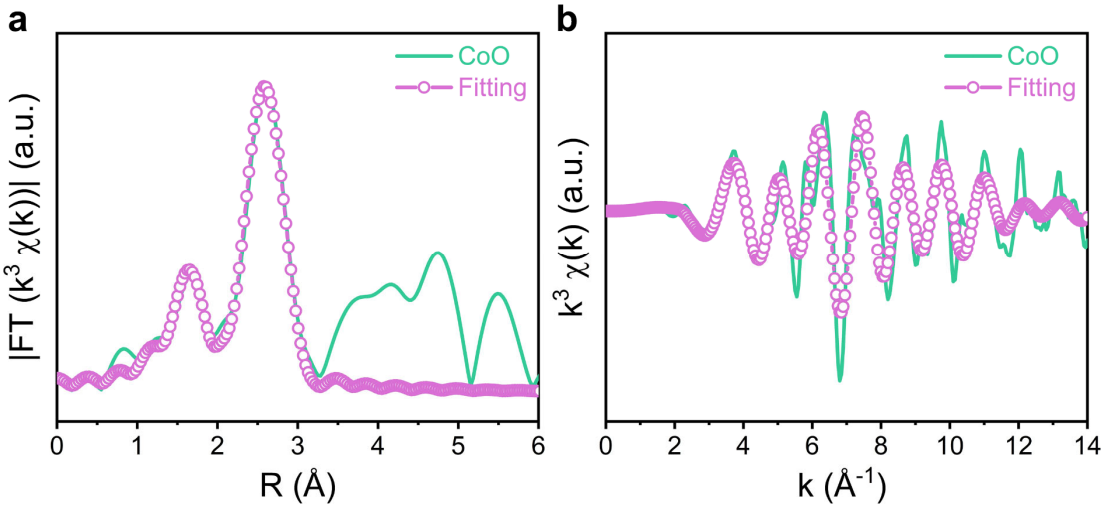

Supplementary Fig. 9 | The least-squares EXAFS fitting results. a, **b** EXAFS fitting curves of CoO in R space (**a**) and k space (**b**), respectively.

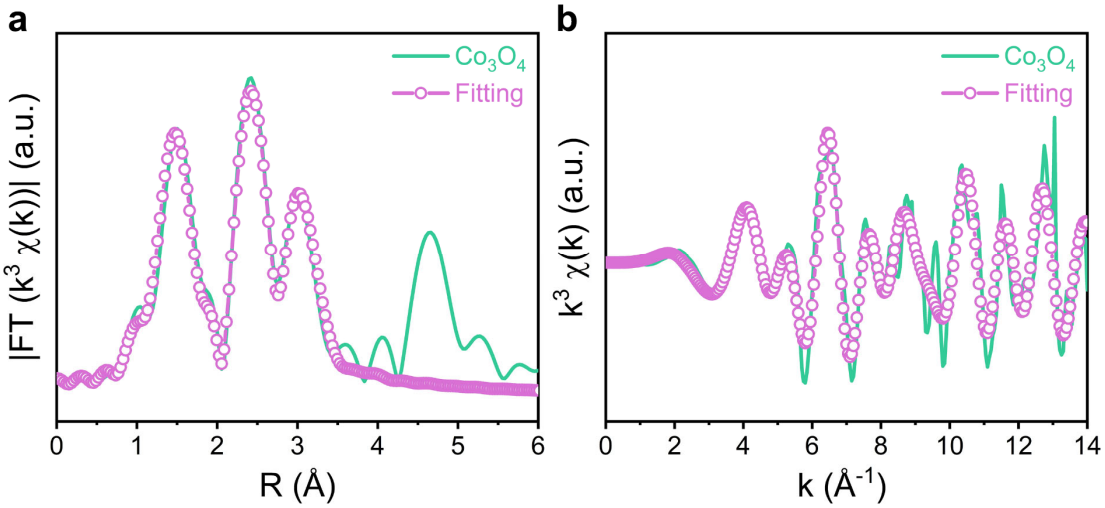

Supplementary Fig. 10 | The least-squares EXAFS fitting results. a, **b** EXAFS fitting curves of Co_3O_4 in R space (**a**) and k space (**b**), respectively.

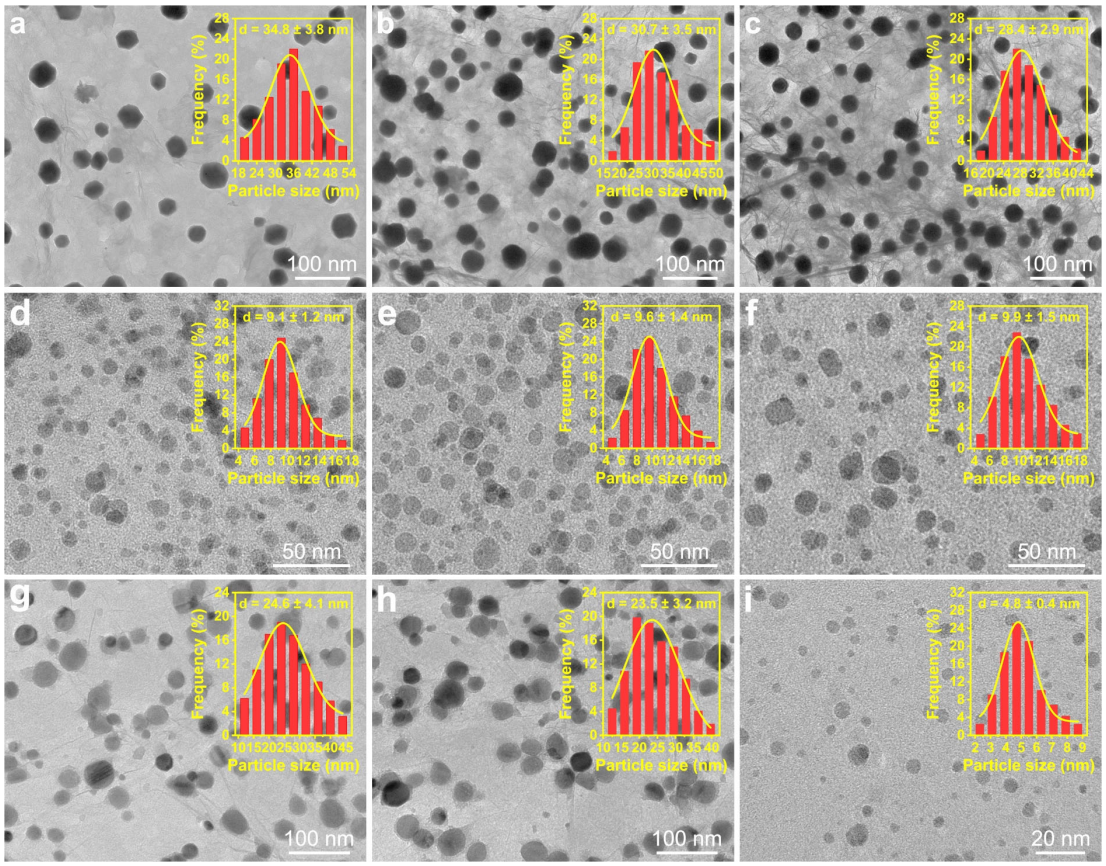

275

276 **Supplementary Fig. 11 | Measured average particle size of Ga-based IMCs.** TEM

277 images of monoclinic $Ni_{13}Ga_9$ IMCs (**a**), hexagonal $Ni_{1.91}Ga$ IMCs (**b**), cubic Ni_3Ga

278 IMCs (**c**), cubic PtGa IMCs (**d**), orthorhombic Pt_5Ga_3 IMCs (**e**), cubic Pt_3Ga IMCs (**f**),

279 orthorhombic Pd_5Ga_3 IMCs (**g**), orthorhombic Pd_2Ga IMCs (**h**), and cubic RhGa IMCs

280 (**i**). The insets present the corresponding size distribution histograms.

281

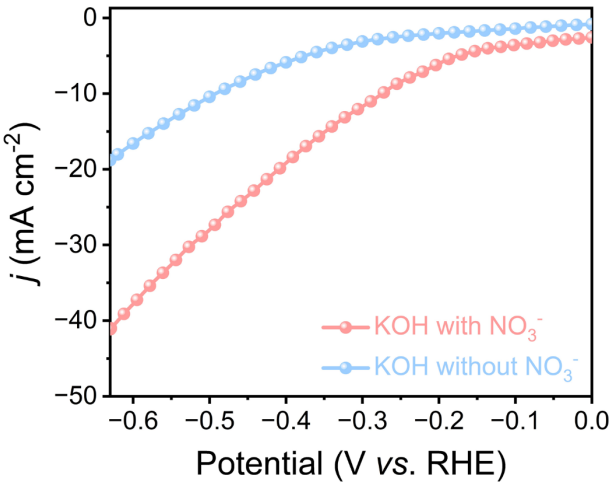

282

283 **Supplementary Fig. 12 | LSV curves.** LSV curves of Co/NG in 0.1 M KOH solution

284 with and without 500 ppm NO_3^--N.

285

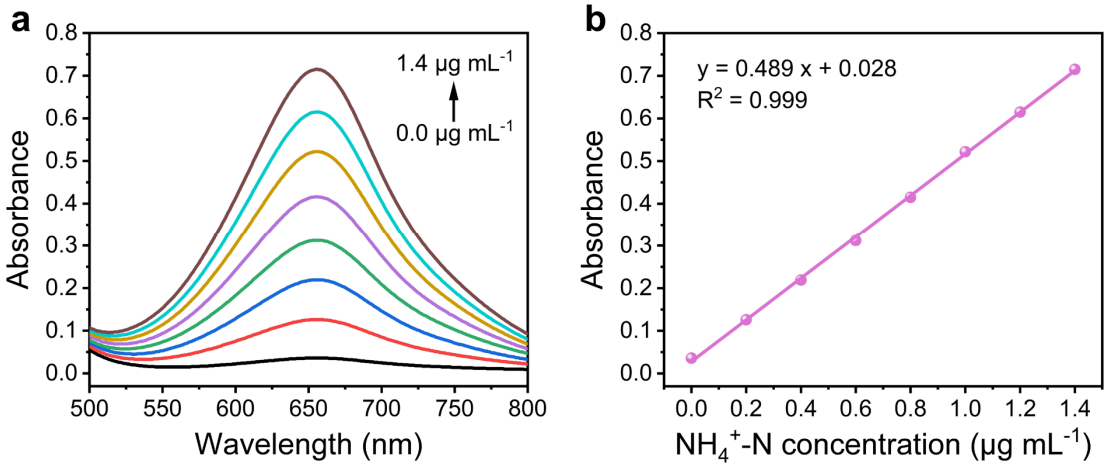

Supplementary Fig. 13 | The UV-Vis calibration curves of NH_4^+ using different concentrations of NH_4Cl solutions as standards. a UV-Vis absorption spectra of standard ammonium solutions with known concentrations in 0.1 M KOH solution. **b** Calibration curve used for determining the NH_4^+-N concentration.

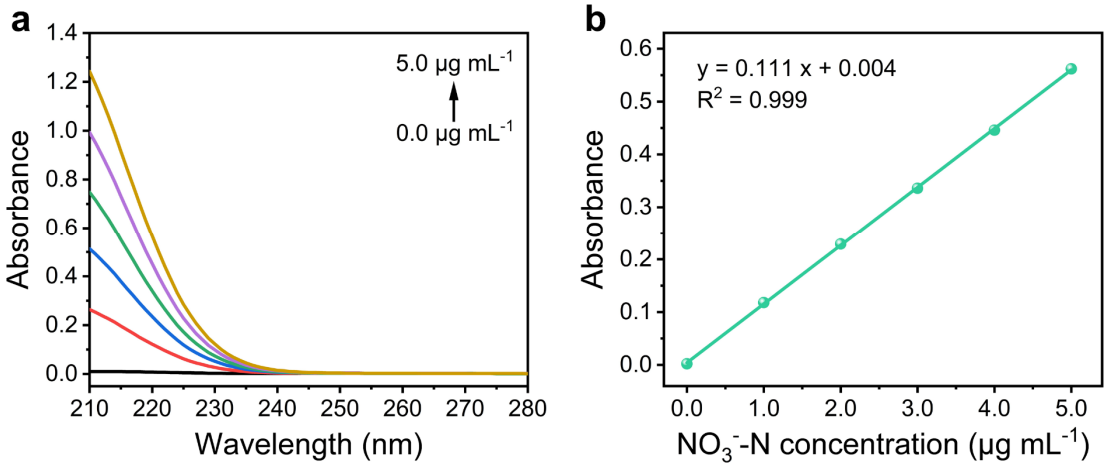

292

293 **Supplementary Fig. 14 | The UV-Vis calibration curves of NO_3^- using different**

294 **concentrations of $NaNO_3$ solutions as standards. a** UV-Vis absorption spectra of

295 standard NO_3^- solutions with known concentrations in 0.1 M KOH solution. **b**

296 Calibration curve used for determining the NO_3^--N concentration.

297

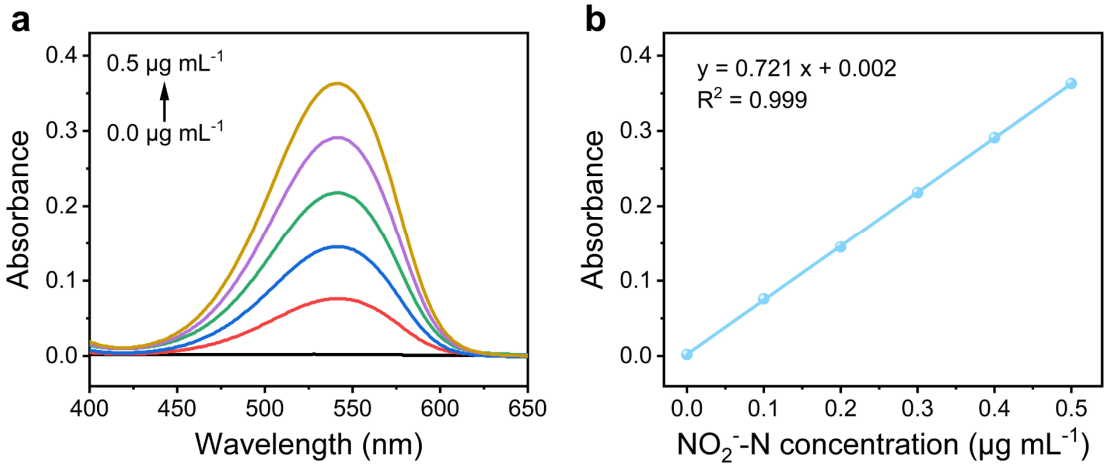

298

299 **Supplementary Fig. 15 | The UV-Vis calibration curves of NO_2^- using different**

300 **concentrations of $NaNO_2$ solutions as standards. a** UV-Vis absorption spectra of

301 standard NO_2^- solutions with known concentrations in 0.1 M KOH solution. **b**

302 Calibration curve used for determining the NO_2^--N concentration.

303

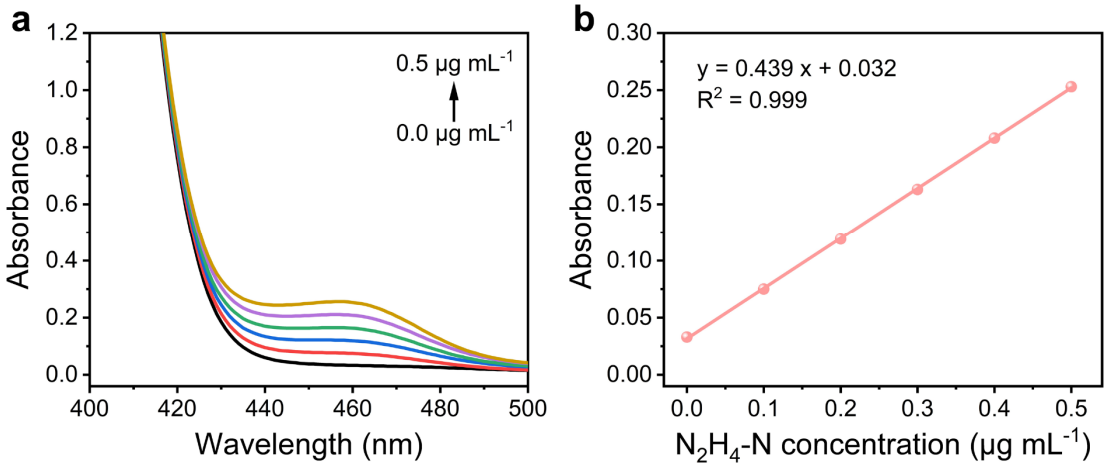

304

305 **Supplementary Fig. 16 | The UV-Vis calibration curves of N_2H_4 using different**

306 **concentrations of N_2H_4 solutions as standards. a** UV-Vis absorption spectra of

307 standard N_2H_4 solutions with known concentrations in 0.1 M KOH solution. **b**

308 Calibration curve used for determining the N_2H_4-N concentration.

309

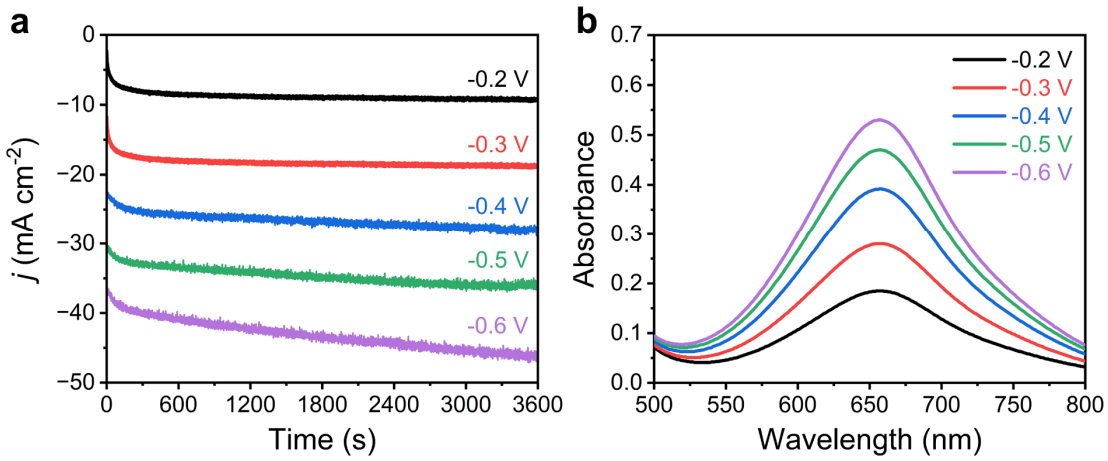

310

311 **Supplementary Fig. 17 | Chronoamperometric curves and UV-Vis spectra for**

312 **quantification of NH_3 concentration. a**, **b** Chronoamperometric curves (**a**) and the

313 corresponding UV-Vis absorption spectra (**b**) of CoGa/NG for NO_3RR at different

314 applied potentials in 0.1 M KOH solution with 500 ppm NO_3^--N.

315

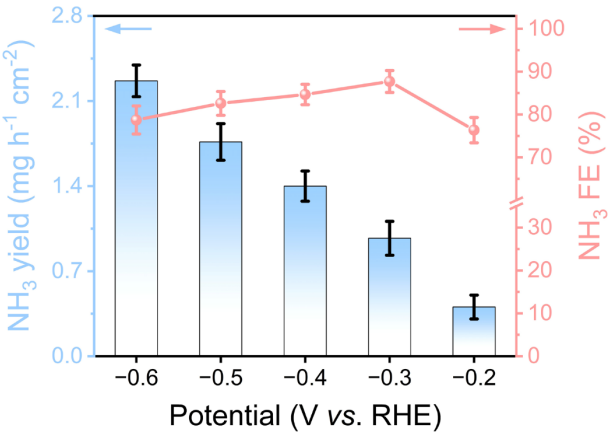

316

317 **Supplementary Fig. 18 | NH_3 yield and NH_3 FE over Co/NG at different applied**

318 **potentials in 0.1 M KOH solution with 500 ppm NO_3^--N.** The error bars indicate the

319 standard deviations calculated from three independent measurements under the same

320 conditions.

321

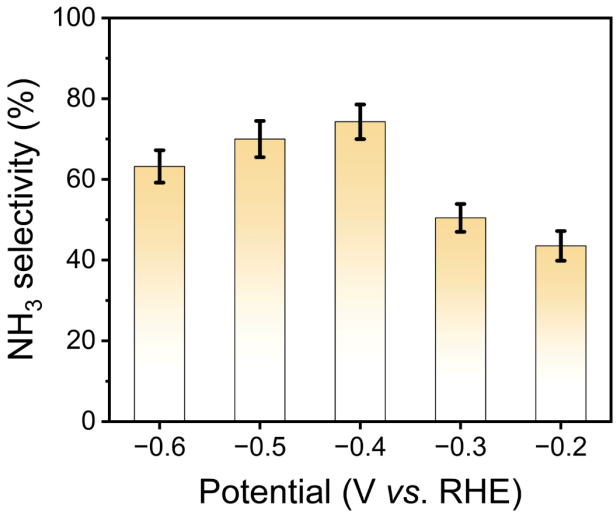

Supplementary Fig. 19 | NH_3 selectivity over Co/NG at different applied potentials in 0.1 M KOH solution with 500 ppm NO_3^--N. The error bars indicate the standard deviations calculated from three independent measurements under the same conditions.

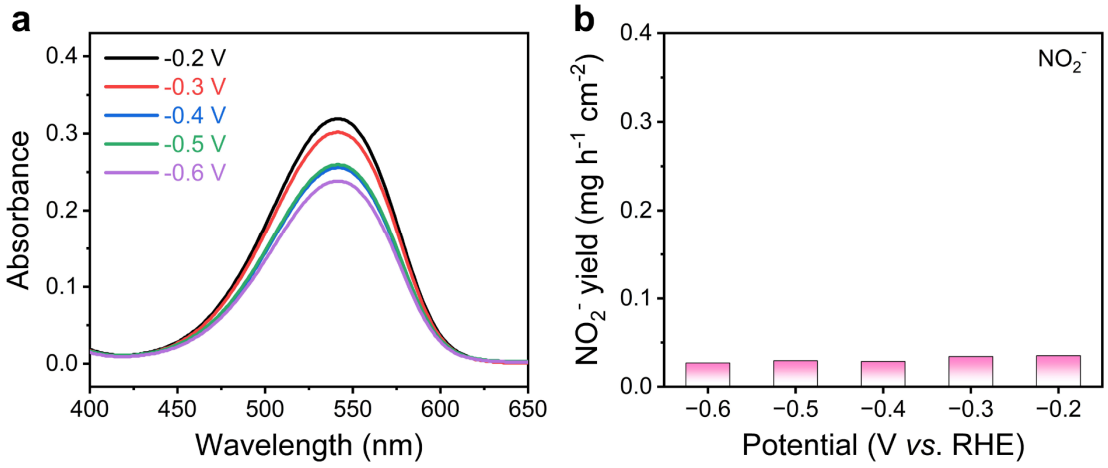

Supplementary Fig. 20 | Quantification of NO_2^- yield by colorimetric method. a, **b** UV-Vis absorption spectra of electrogenerated NO_2^- (**a**) and the corresponding NO_2^- yield (**b**) over CoGa/NG at different applied potentials in 0.1 M KOH solution with 500 ppm NO_3^--N.

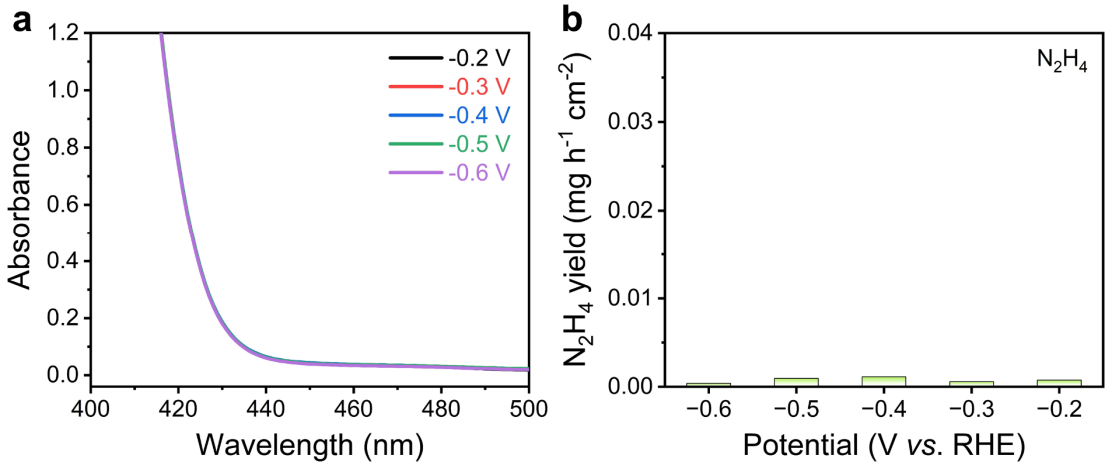

333

334 **Supplementary Fig. 21 | Quantification of N_2H_4 yield by colorimetric method. a**, **b**

335 UV-Vis absorption spectra of electrogenerated N_2H_4 (**a**) and the corresponding N_2H_4

336 yield (**b**) over CoGa/NG at different applied potentials in 0.1 M KOH solution with 500

337 ppm NO_3^--N.

338

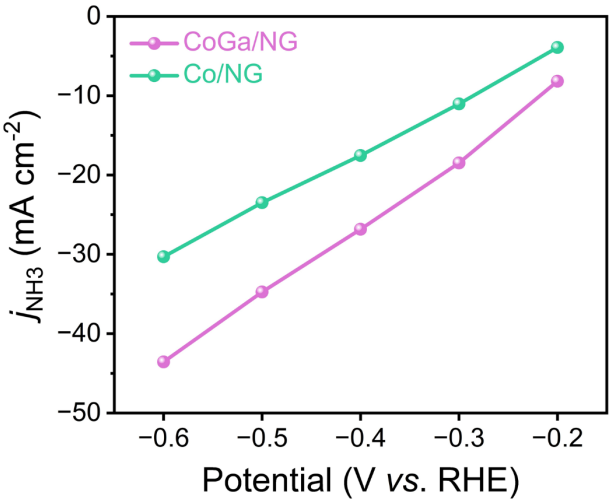

Supplementary Fig. 22 | Comparison of NH_3 partial current densities (j_{NH3}) for CoGa/NG and Co/NG. The j_{NH3} of CoGa/NG is more negative than that of Co/NG at different applied potentials in 0.1 M KOH solution with 500 ppm NO_3^--N, which suggests that the CoGa/NG exhibits excellent NH_3 activity.

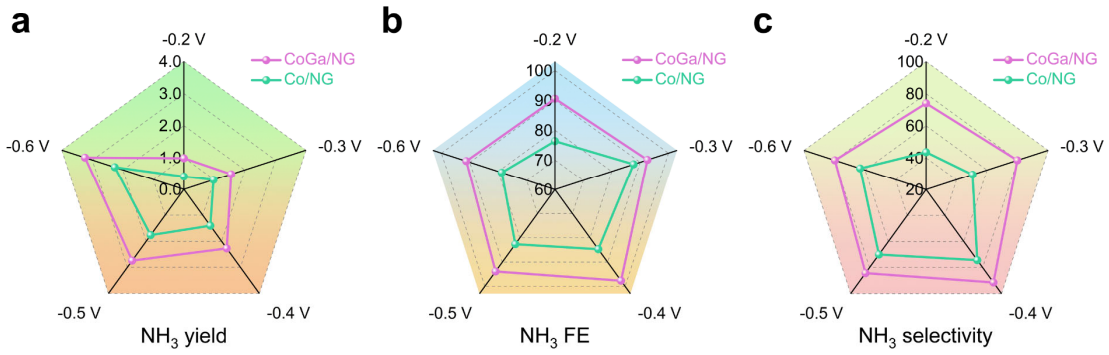

345

346 **Supplementary Fig. 23 | Performance comparison of different catalysts. a-c** NH_3

347 yield (**a**), NH_3 FE (**b**), and NH_3 selectivity (**c**) for CoGa/NG and Co/NG at different

348 applied potentials in 0.1 M KOH solution with 500 ppm NO_3^--N.

349

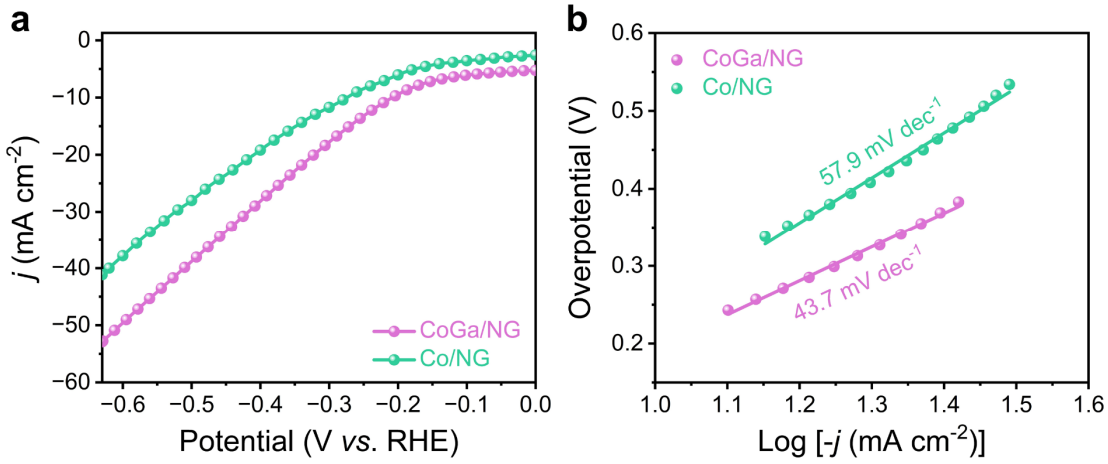

350

351 **Supplementary Fig. 24 | LSV curves and Tafel plots. a** LSV curves of CoGa/NG and

352 Co/NG in 0.1 M KOH solution with 500 ppm NO_3^--N. **b** The corresponding Tafel plots

353 derived from (**a**).

354

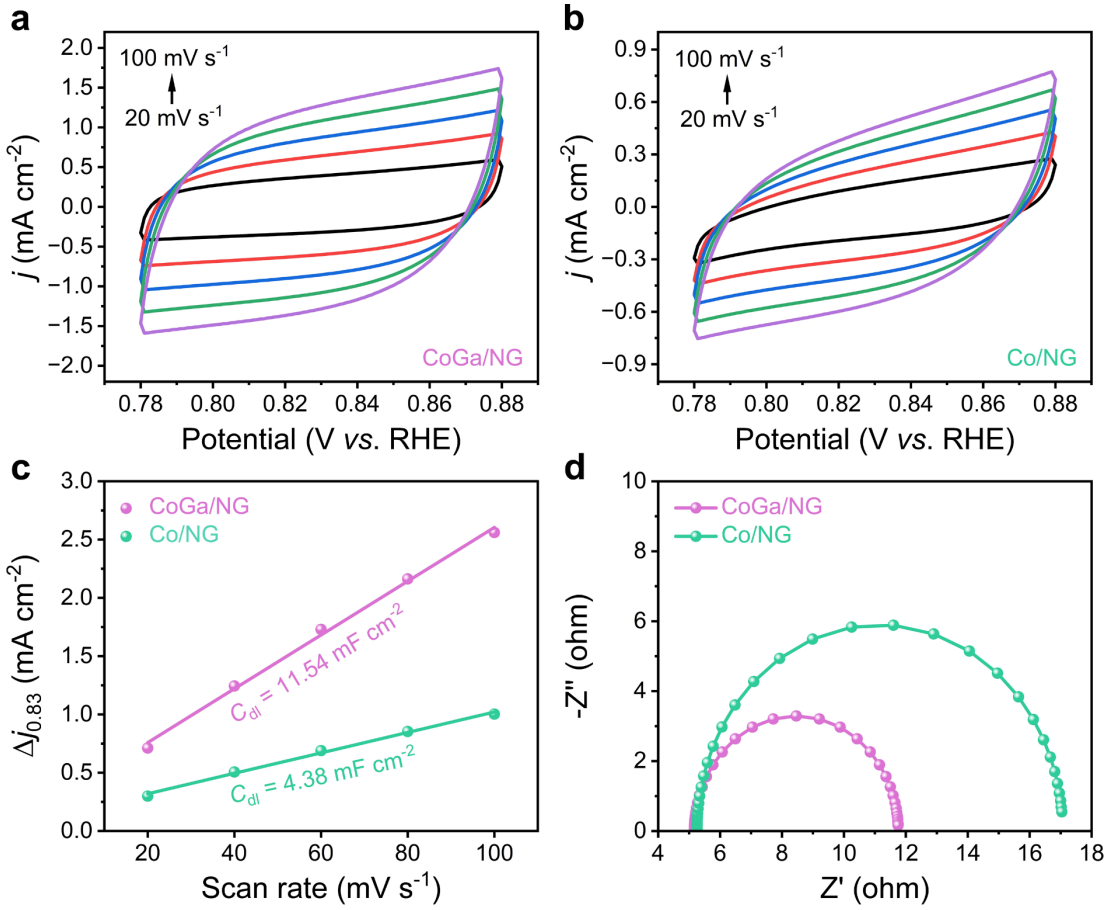

355

356 **Supplementary Fig. 25 | Electrochemically active surface areas (ECSAs) and**

357 **electrochemical impedance spectroscopy (EIS). a**, **b** CV curves of CoGa/NG (**a**) and

358 Co/NG (**b**) with various scan rates from 20 to 100 mV s^{-1} in 0.1 M KOH solution with

359 500 ppm NO_3^--N. **c** The calculated C_{dl} values for CoGa/NG and Co/NG. **d** Nyquist plots

360 of CoGa/NG and Co/NG.

361

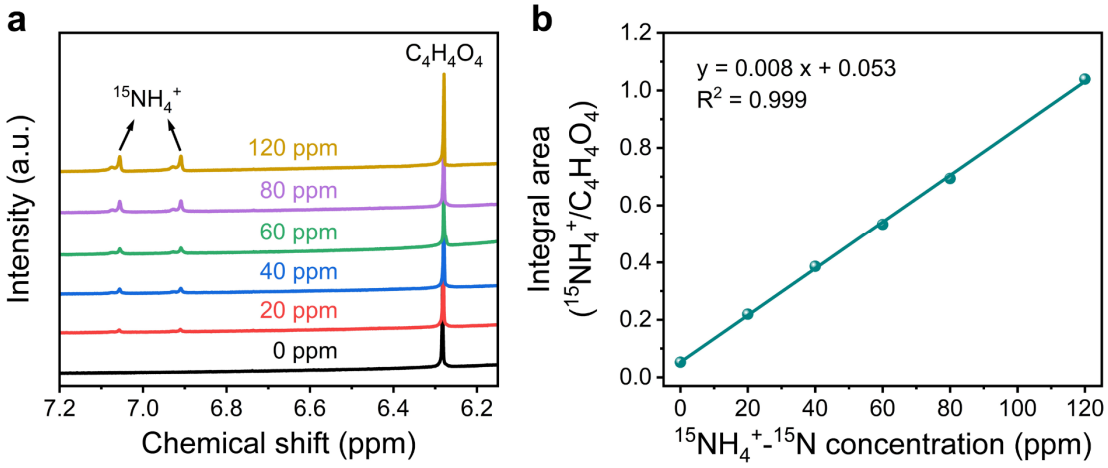

362

363 **Supplementary Fig. 26 | The ^{1}H NMR calibration curves of $^{15}NH_4^+$ using different**

364 **concentrations of $^{15}NH_4Cl$ solutions with $C_4H_4O_4$ as standards. a** ^{1}H NMR spectra

365 of $^{15}NH_4^+$ standard solution with different concentrations in 0.1 M KOH solution. **b**

366 Standard curve of integral area ($^{15}NH_4^+/C_4H_4O_4$) against $^{15}NH_4^+$-^{15}N concentration.

367

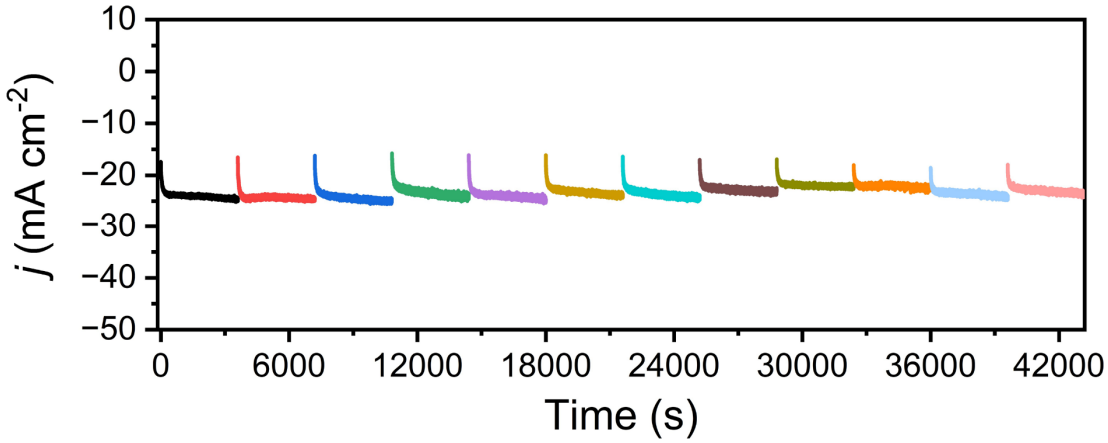

368

369 **Supplementary Fig. 27 | Stability tests of CoGa/NG.** Time-dependent current density

370 curves during 12 consecutive cycles over CoGa/NG for NO_3RR at the applied potential

371 of -0.4 V in 0.1 M KOH solution with 500 ppm NO_3^--N.

372

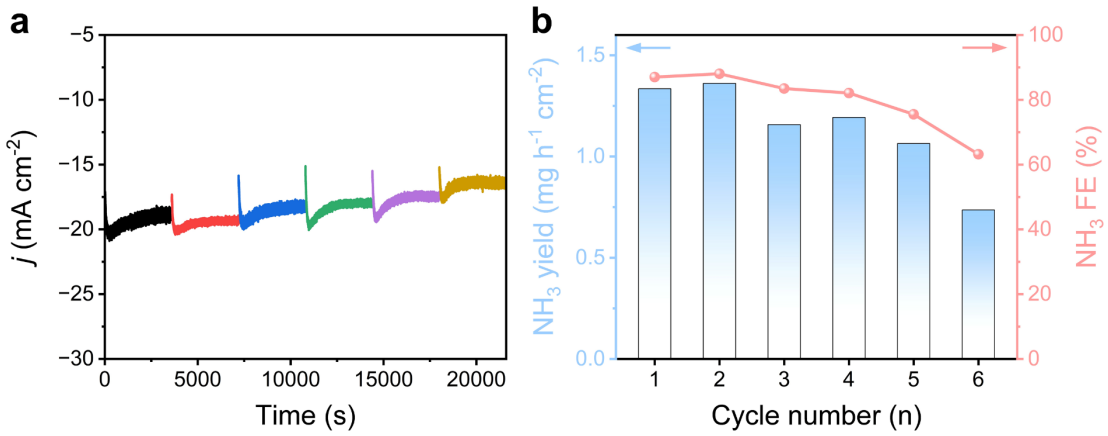

373

374 **Supplementary Fig. 28 | Stability tests of Co/NG. a** Time-dependent current density

375 curves. **b** The corresponding NH_3 yield and NH_3 FE during 6 consecutive cycles over

376 Co/NG for NO_3RR at the applied potential of -0.4 V in 0.1 M KOH solution with 500

377 ppm NO_3^--N.

378

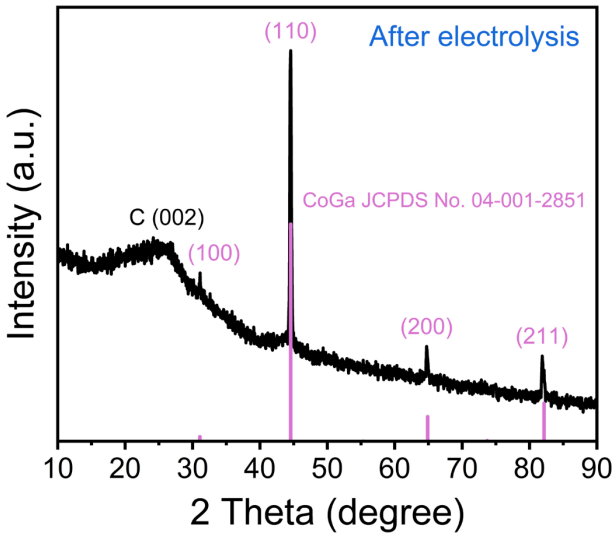

379

380 **Supplementary Fig. 29 | XRD pattern.** XRD pattern of CoGa/NG after the long-term

381 stability tests in 0.1 M KOH solution with 500 ppm NO_3^--N.

382

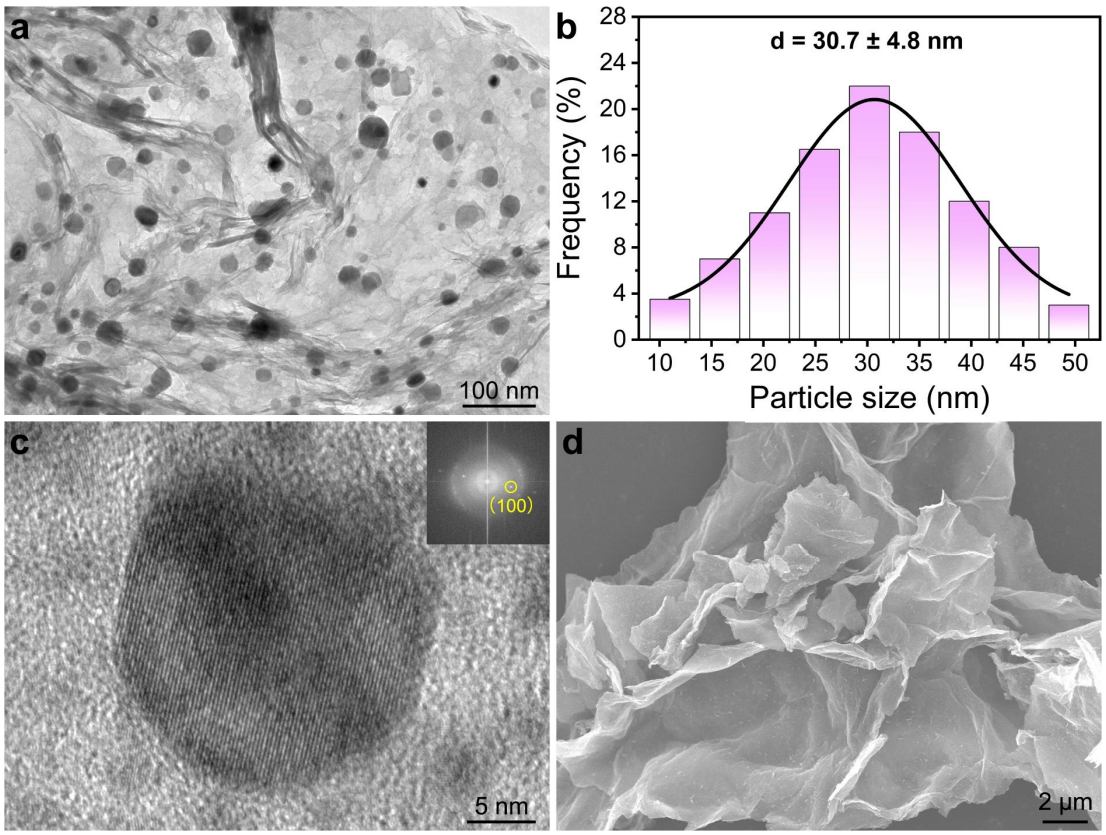

Supplementary Fig. 30 | Morphology and structure characterizations of CoGa/NG after the long-term stability tests. TEM image (**a**), the corresponding particle size distribution histogram (**b**), HRTEM image (**c**), and SEM image (**d**) of CoGa/NG after the long-term stability tests.

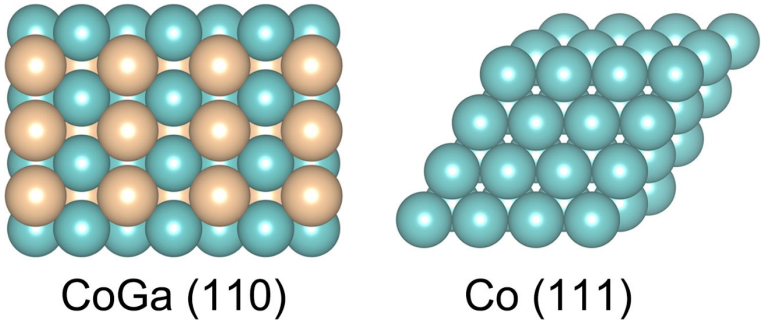

Supplementary Fig. 31 | The optimized structural models of CoGa (110) and Co (111). The orange and cyan spheres represent Ga and Co atoms, respectively.

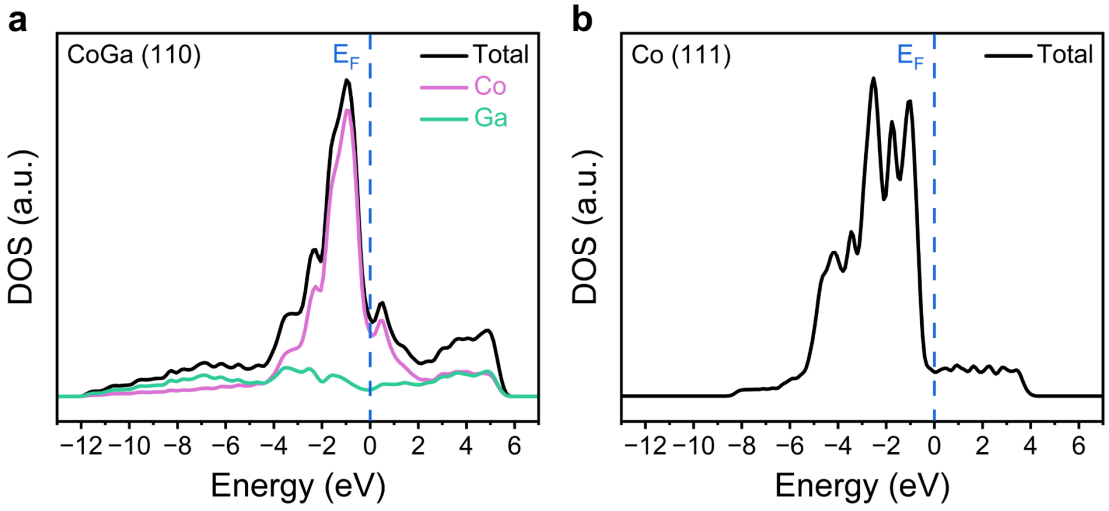

393

394 **Supplementary Fig. 32 | Electronic structures. a**, **b** The DOSs of CoGa (110) (**a**) and

395 Co (111) (**b**).

396

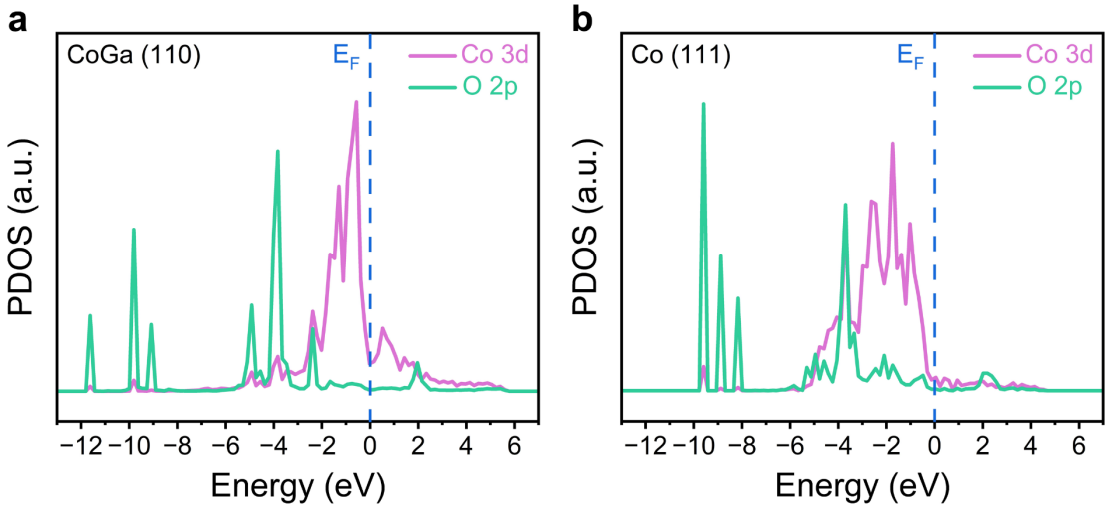

397

398 **Supplementary Fig. 33 | Electronic structures. a**, **b** The PDOS profiles of Co 3d and

399 O 2p of *NO_3 intermediate on CoGa (110) (**a**) and Co (111) (**b**).

400

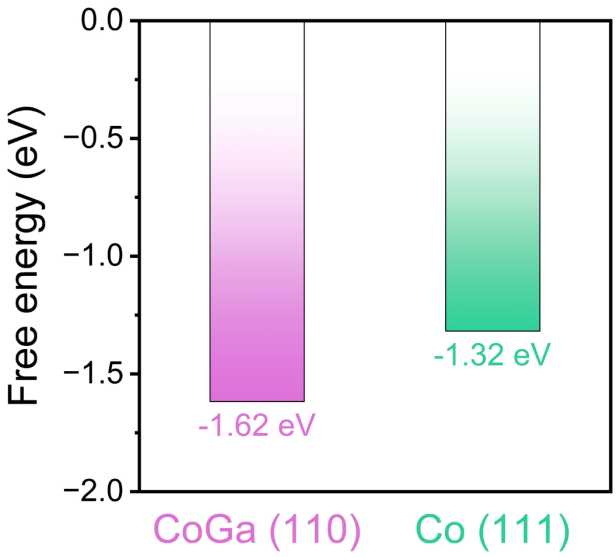

Supplementary Fig. 34 | The free energy diagrams of *NO_3 adsorption on CoGa (110) and Co (111). The free energy of *NO_3 adsorption on CoGa (110) is calculated to be -1.62 eV, which is more negative compared to that on Co (111) (-1.32 eV). Such an apparent difference in free energy of *NO_3 adsorption indicates a stronger adsorption capacity of *NO_3 intermediate on CoGa (110), which plays a vital role in facilitating the subsequent reduction process.

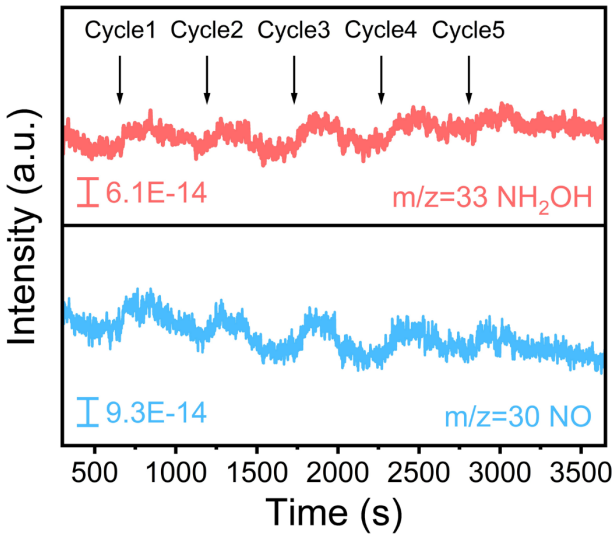

409

410 **Supplementary Fig. 35 | DEMS measurements.** The m/z signals of 33 and 30 are

411 indexed to NH_2OH and NO, respectively.

412

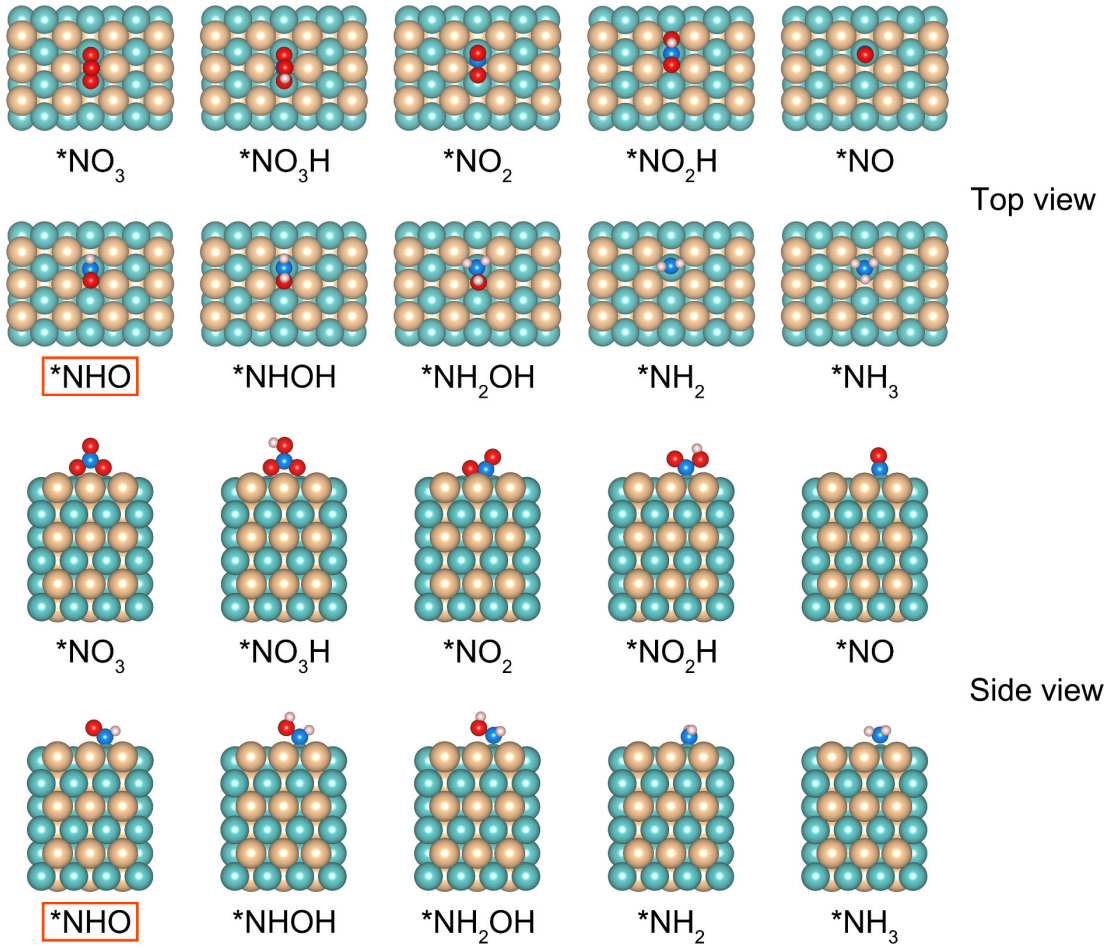

413

414 **Supplementary Fig. 36 | The optimized structural models of reaction intermediates**

415 **involved in the NHO pathway of the NO_3RR process on CoGa (110).** The pink, blue,

416 red, orange and cyan spheres represent H, N, O, Ga and Co atoms, respectively.

417

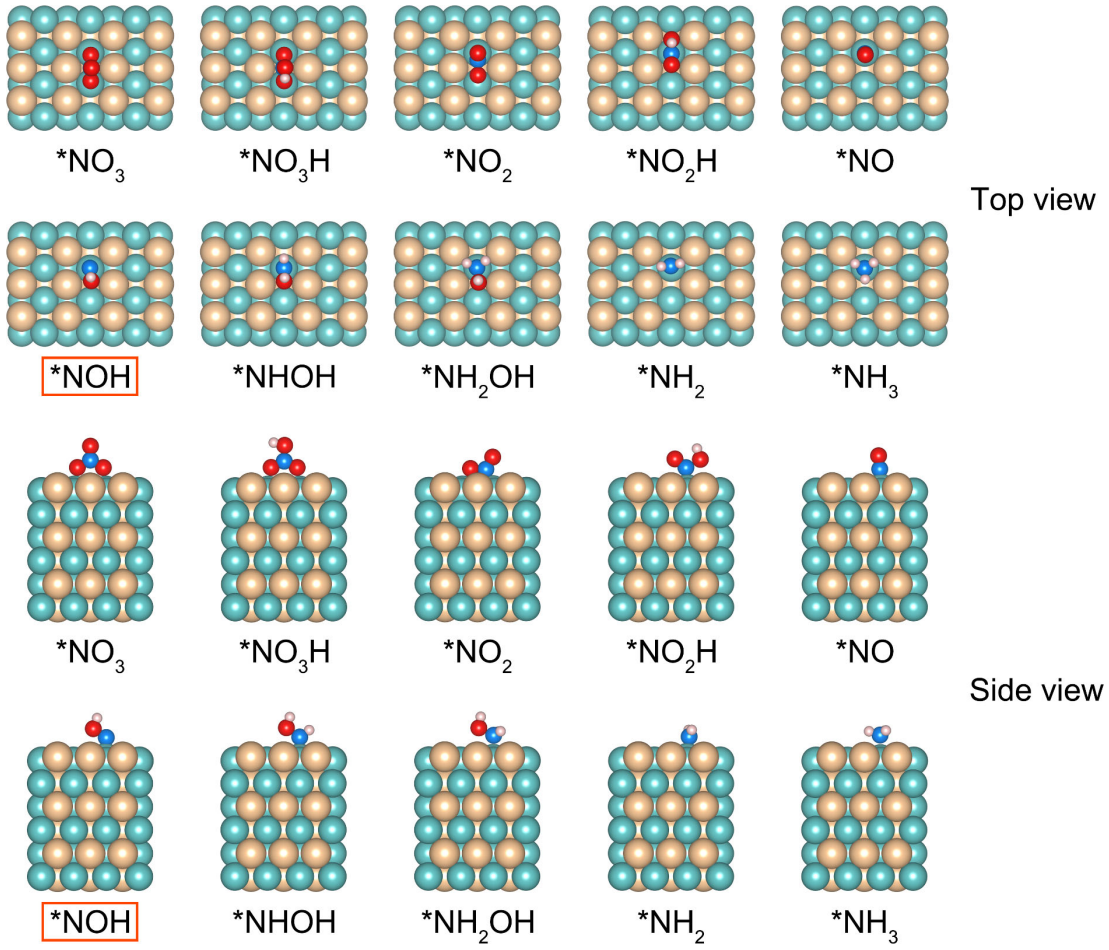

418

419 **Supplementary Fig. 37 | The optimized structural models of reaction intermediates**

420 **involved in the NOH pathway of the NO_3RR process on CoGa (110).** The pink, blue,

421 red, orange and cyan spheres represent H, N, O, Ga and Co atoms, respectively.

422

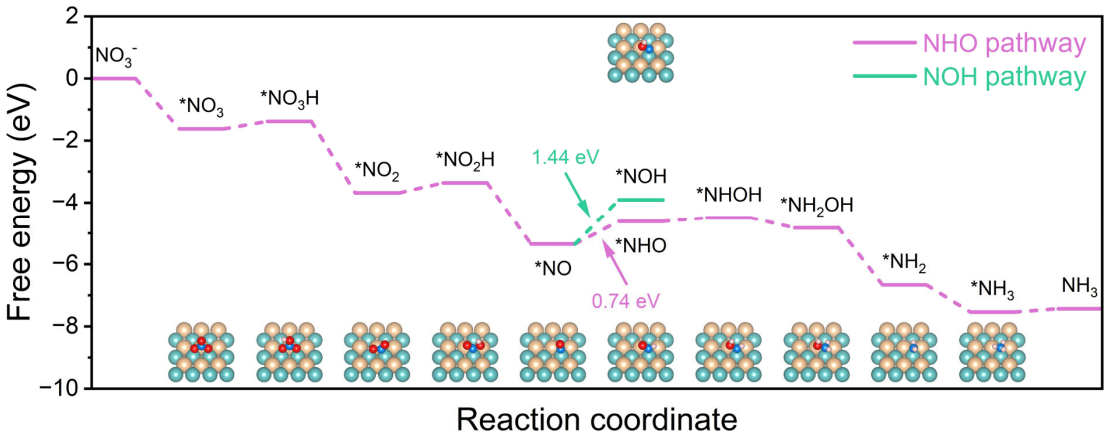

423

424 **Supplementary Fig. 38 | The free energy diagrams of the NO_3RR process on CoGa**

425 **(110).** The pink, blue, red, orange and cyan spheres represent H, N, O, Ga and Co atoms,

426 respectively.

427

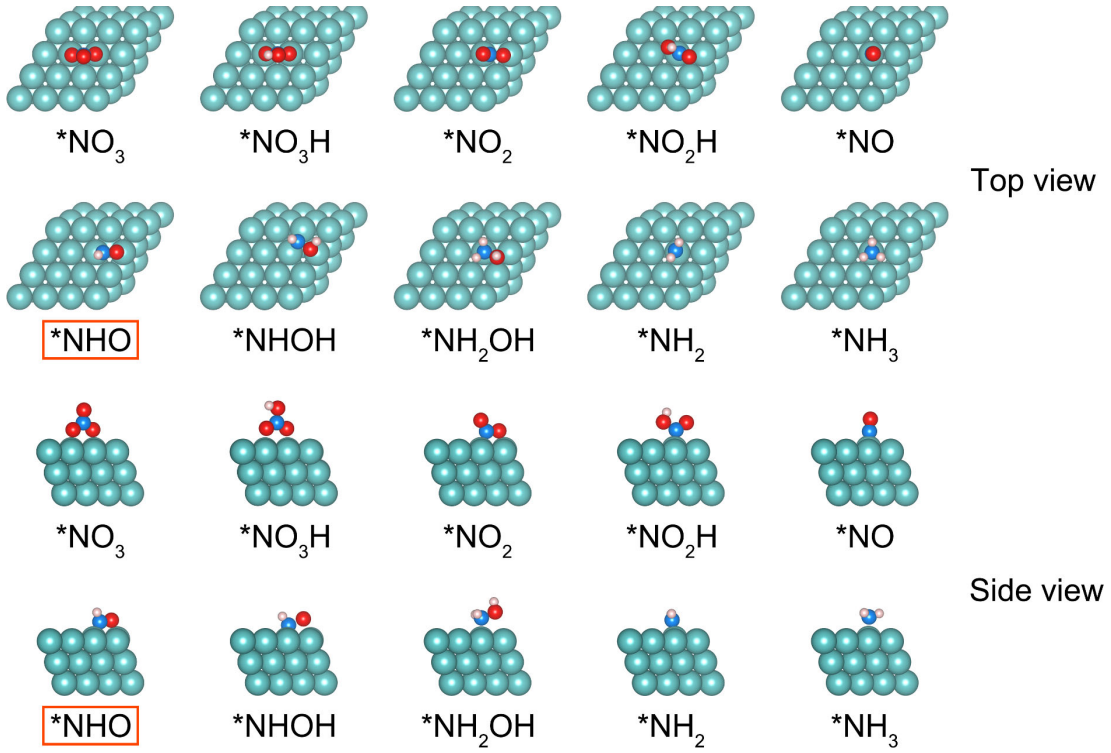

Supplementary Fig. 39 | The optimized structural models of reaction intermediates involved in the NHO pathway of the NO_3RR process on Co (111). The pink, blue, red and cyan spheres represent H, N, O and Co atoms, respectively.

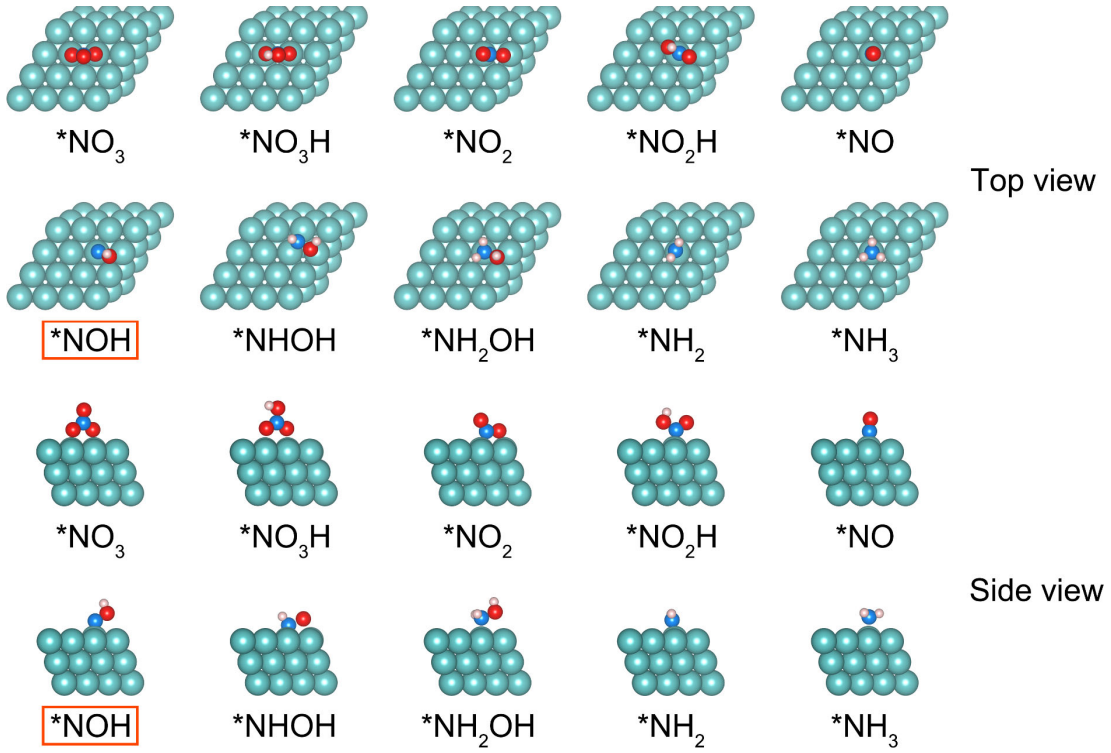

433

434 **Supplementary Fig. 40 | The optimized structural models of reaction intermediates**

435 **involved in the NOH pathway of the NO_3RR process on Co (111).** The pink, blue,

436 red and cyan spheres represent H, N, O and Co atoms, respectively.

437

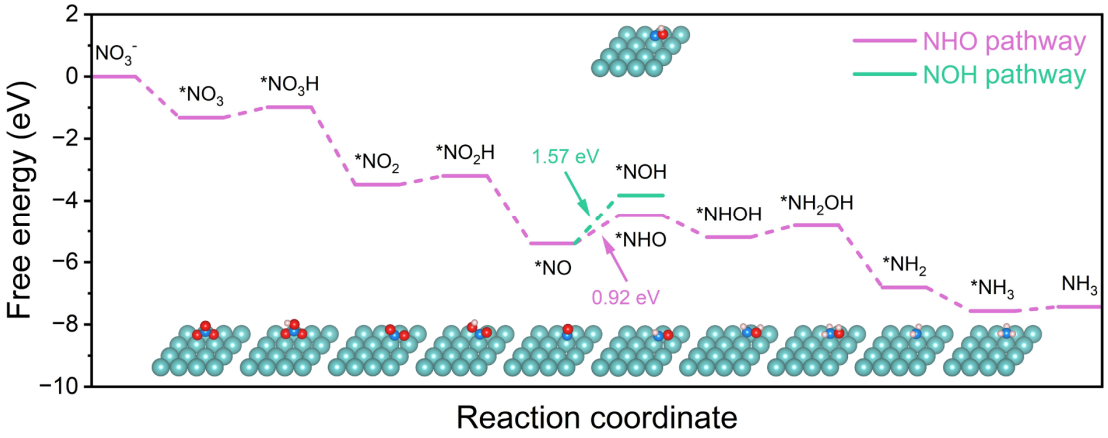

438

439 **Supplementary Fig. 41 | The free energy diagrams of the NO_3RR process on Co**

440 **(111).** The pink, blue, red and cyan spheres represent H, N, O and Co atoms,

441 respectively.

442

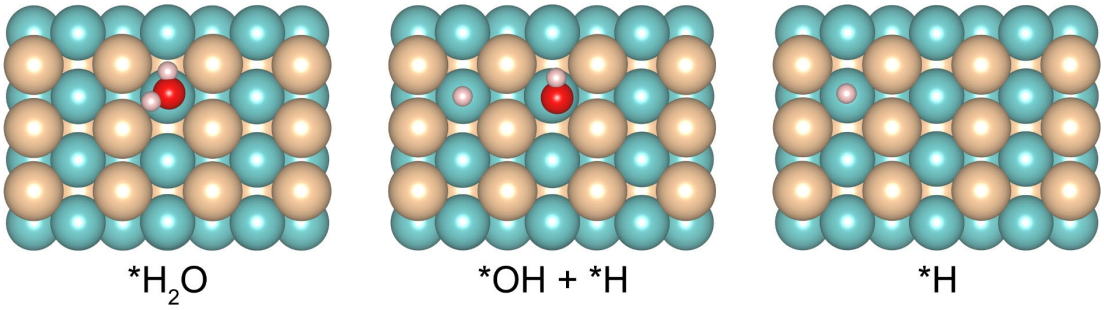

443

444 **Supplementary Fig. 42 | The optimized structural models of reaction intermediates**

445 **involved in the alkaline HER process on CoGa (110).** The pink, red, orange and cyan

446 spheres represent H, O, Ga and Co atoms, respectively.

447

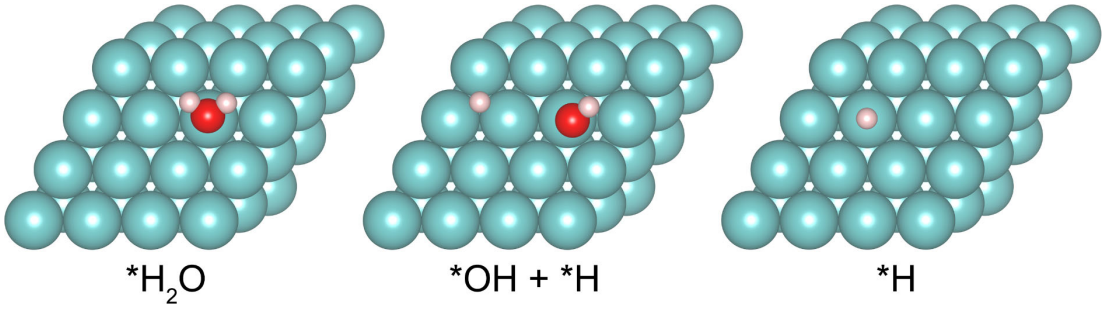

Supplementary Fig. 43 | The optimized structural models of reaction intermediates involved in the alkaline HER process on Co (111). The pink, red and cyan spheres represent H, O and Co atoms, respectively.

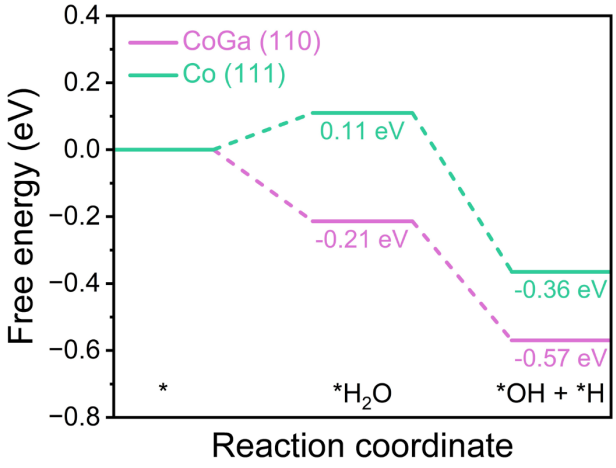

453

454 **Supplementary Fig. 44 | The free energy diagrams of H_2O dissociation on CoGa**

455 **(110) and Co (111).** CoGa (110) greatly facilitates the processes of H_2O adsorption and

456 dissociation compared to Co (111), which indicates a more favorable proton production.

457

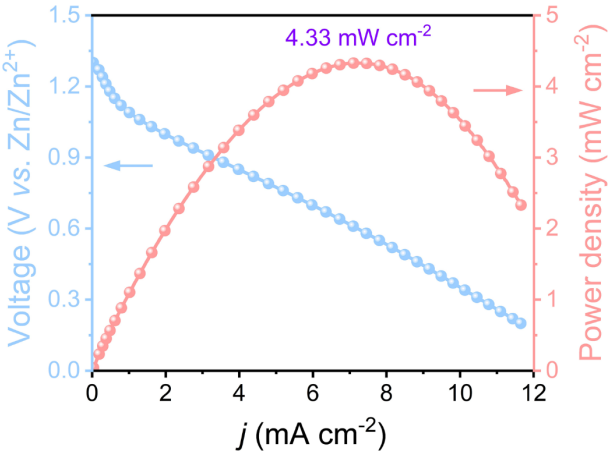

458

459 **Supplementary Fig. 45 | The performance of the Co/NG-based Zn-NO_3^- battery.**

460 The discharging polarization curve and the resultant power density of the Co/NG-based

461 Zn-NO_3^- battery.

462

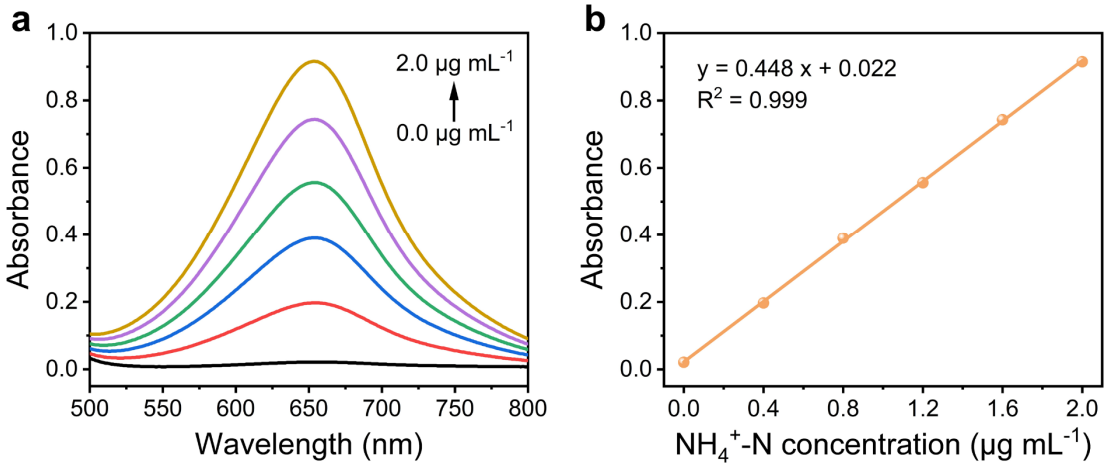

463

464 **Supplementary Fig. 46 | The UV-Vis calibration curves of NH_4^+ using different**

465 **concentrations of NH_4Cl solutions as standards. a** UV-Vis absorption spectra of

466 standard ammonium solutions with known concentrations in 1.0 M KOH solution. **b**

467 Calibration curve used for determining the NH_4^+-N concentration.

468

Supplementary Tables

Supplementary Table 1 | Cell parameters of CoGa IMCs determined from the XRD data.

CoGa IMCs	
Space group	$Pm\bar{3}m$
a	2.869 Å
b	2.869 Å
c	2.869 Å
α	90°
β	90°
γ	90°

Supplementary Table 2 | Mass and atomic percentages of Co and Ga elements obtained from ICP-AES.

Catalysts	Co (wt.%)	Ga (wt.%)	Co/Ga (at.%)
CoGa/NG	14.40	15.62	52.17:47.83
Co/NG	15.58	N/A	N/A

Supplementary Table 3 | EXAFS fitting parameters at the Co K-edge for various samples (S_0^2=0.78).

Sample	Path	CN	R (Å)	σ^2 (Å^2)	ΔE_0 (eV)	R factor (%)
Co foil	Co-Co	12	2.49±0.01	0.0036	7.3±0.3	0.0076
CoO	Co-O	6	2.11±0.01	0.0058	-4.4±1.0	0.0073
	Co-Co	12	3.00±0.01	0.0108		
Co_3O_4	Co-O	5.3	1.92±0.01	0.0024	-6.1±0.8	0.0134
	Co-Co	4	2.86±0.01	0.0029		
	Co-Co	8	3.37±0.01	0.0058		
CoGa/NG	Co-O	4.0±0.4	2.05±0.02	0.0127	5.4±2.5	0.0039
	Co-Ga	7.9±0.4	2.38±0.03	0.0091		

S_0^2 is the amplitude reduction factor; CN is the coordination number; R is the interatomic distance (the bond length between central atoms and surrounding coordination atoms); σ^2 is the Debye-Waller factor (a measure of thermal and static disorder in absorber-scatter distances); ΔE_0 is the edge-energy shift (the difference between the zero kinetic energy value of the sample and that of the theoretical model). R factor is used to value the goodness of the fitting.

Supplementary Table 4 | Cell parameters of Ga-based IMCs determined from the XRD data.

Sample	Space group	a	b	c	α	β	γ
$Ni_{13}Ga_9$ IMCs	*C*12/*m*1	13.83 Å	7.902 Å	8.478 Å	90°	35.9°	90°
$Ni_{1.91}Ga$ IMCs	$P6_3/mmc$	3.999 Å	3.999 Å	5.001 Å	90°	90°	120°
Ni_3Ga IMCs	$Pm\bar{3}m$	3.591 Å	3.591 Å	3.591 Å	90°	90°	90°
PtGa IMCs	$P2_13$	4.912 Å	4.912 Å	4.912 Å	90°	90°	90°
Pt_5Ga_3 IMCs	*Cmmm*	8.050 Å	7.405 Å	3.947 Å	90°	90°	90°
Pt_3Ga IMCs	$Pm\bar{3}m$	3.911 Å	3.911 Å	3.911 Å	90°	90°	90°
Pd_5Ga_3 IMCs	*Pbam*	5.440 Å	10.55 Å	4.026 Å	90°	90°	90°
Pd_2Ga IMCs	*Pnma*	5.482 Å	4.056 Å	7.790 Å	90°	90°	90°
RhGa IMCs	$Pm\bar{3}m$	3.001 Å	3.001 Å	3.001 Å	90°	90°	90°

Supplementary Table 5 | Comparison of NO_3RR performances over CoGa/NG with recently reported electrocatalysts.

Catalyst	Electrolyte	NH_3 yield	NH_3 FE	Ref.
CoGa/NG	**0.1 M KOH (500 ppm NO_3^--N)**	**3.24 mg h^{-1} cm^{-2}**	**97.7%**	**This work**
Fe/Cu-HNG	1 M KOH (1400 ppm NO_3^--N)	18.36 mg h^{-1} mg^{-1}	92.5%	*Nat. Commun.* **14**, 3634 (2023)
FTO-E	PBS (1400 ppm NO_3^--N)	12.41 mg h^{-1} $mg^{-1}_{cat.}$	87.6%	*Angew. Chem. Int. Ed.* **62**, e202215782 (2023)
PdCu-H	0.1 M KOH (140 ppm NO_3^--N)	9.37 mg h^{-1} mg^{-1}	87.3%	*Small* **19**, 2300794 (2023)
Ru_1Cu_{10}/rGO	1 M KOH (1400 ppm NO_3^--N)	6.46 mg h^{-1} cm^{-2}	98%	*Adv. Mater.* **35**, 2202952 (2023)
Cu-N-C SAC	0.1 M KOH (1400 ppm NO_3^--N)	4.50 mg h^{-1} cm^{-2}	84.7%	*J. Am. Chem. Soc.* **144**, 12062 (2022)
Fe/Ni_2P	0.2 M K_2SO_4 (700 ppm NO_3^--N)	4.17 mg h^{-1} cm^{-2}	94.3%	*Adv. Energy Mater.* **12**, 2103872 (2022)
Cu/Cu_2O NWAs	0.5 M Na_2SO_4 (200 ppm NO_3^--N)	4.16 mg h^{-1} cm^{-2}	95.8	*Angew. Chem. Int. Ed.* **59**, 5350 (2020)
PR-CuNC	0.1 M KOH (1400 ppm NO_3^--N)	3.74 mg h^{-1} cm^{-2}	94.6%	*Appl. Catal. B* **340**, 123228 (2024)
NiPr-TPA-COF	0.5 M Na_2SO_4 (1400 ppm NO_3^--N)	2.50 mg h^{-1} cm^{-2}	90%	*Energy Environ. Sci.* **16**, 201, (2023)
CoNi-Vp-1.0	0.5 M Na_2SO_4 (50 ppm NO_3^--N)	1.66 mg h^{-1} cm^{-2}	84.3%	*Appl. Catal. B* **330**, 122627 (2023)
Pd/TiO_2	1 M LiCl (3500 ppm NO_3^--N)	1.12 mg h^{-1} cm^{-2}	92.1%	*Energy Environ. Sci.* **14**, 3938 (2021)
$CoMn_2O_4$/NC	0.1 M Na_2SO_4 (1400 ppm NO_3^--N)	1.04 mg h^{-1} cm^{-2}	92.4%	*Appl. Catal. B* **322**, 122090 (2023)
Co-Fe@Fe_2O_3	0.1 M Na_2SO_4 (500 ppm NO_3^--N)	0.88 mg h^{-1} cm^{-2}	85.2%	*Proc. Natl. Acad. Sci. U.S.A.* **119**, e2115504119 (2022)
O-Cu-PTCDA	0.1 M PBS (500 ppm NO_3^-)	0.44 mg h^{-1} cm^{-2}	85.9%	*Nat. Energy* **5**, 605 (2020)
Co-CNP	0.02 M Na_2SO_4 (100 ppm NO_3^--N)	0.43 mg h^{-1} cm^{-2}	92.0%	*Proc. Natl. Acad. Sci. U.S.A.* **119**, e2123450119 (2022)

Supplementary Table 6 | The comparison of NH_3 yield and power density of the CoGa/NG-based Zn-NO_3^- battery with the recently reported Zn-NO_3^- battery.

Catalyst	NH_3 yield (mg h^{-1} cm^{-2})	Power density (mW cm^{-2})	Ref.
CoGa/NG	**1.58**	**10.58**	**This work**
Pd/TiO_2	0.54	0.87	*Energy Environ. Sci.* **14**, 3938 (2021)
CoNi-Vp-1.0	0.21	1.05	*Appl. Catal. B* **330**, 122627 (2023)
RuFe NFs	N/A	1.9	*Proc. Natl. Acad. Sci. U.S.A.* **120**, e2306461120 (2023)
Fe/Ni_2P	0.38	3.25	*Adv. Energy Mater.* **12**, 2103872 (2022)
Co_2AlO_4/CC	0.75	3.43	*Chem. Eng. J.* **435**, 135104 (2022)
NiCoBDC@HsGDY	1.13	3.66	*ACS Nano* **17**, 6687 (2023)
$NiCo_2O_4$/CC	0.82	3.94	*Small* **18**, 2106961 (2022)
Ni-NPs-1.6	N/A	4.2	*Energy Environ. Sci.* **16**, 2611 (2023)
PdCu-P	N/A	4.9	*Small* **19**, 2300794 (2023)
Ir SAC-Co_3O_4	0.76	5.6	*Chem Catal.* **3**, 100477 (2023)
MP-Cu	1.29	7.56	*Adv. Funct. Mater.* **33**, 2212236 (2023)
0.6W-O-CoP@NF	2.79	9.27	*Adv. Mater.* **35**, 2304508 (2023)
ISAA In-Pdene	0.92	12.64	*J. Am. Chem. Soc.* **145**, 13957 (2023)

N/A: Not available.

Supplementary References

1. Kresse G., Furthmüller J. Efficient iterative schemes for ab initio total-energy calculations using a plane-wave basis set. *Phys. Rev. B* **54**, 11169-11186 (1996).
2. Kresse G., Hafner J. Ab initio molecular dynamics for liquid metals. *Phys. Rev. B* **47**, 558-561 (1993).
3. Hammer B., Hansen L. B., Nørskov J. K. Improved adsorption energetics within density-functional theory using revised Perdew-Burke-Ernzerhof functionals. *Phys. Rev. B* **59**, 7413-7421 (1999).
4. Perdew J. P., Burke K., Ernzerhof M. Generalized gradient approximation made simple. *Phys. Rev. Lett.* **77**, 3865-3868 (1996).
5. Blöchl P. E. Projector augmented-wave method. *Phys. Rev. B* **50**, 17953-17979 (1994).
6. Klimeš J., Bowler D. R., Michaelides A. Van der Waals density functionals applied to solids. *Phys. Rev. B* **83**, 195131 (2011).
7. Grimme S., Antony J., Ehrlich S., Krieg H. A consistent and accurate ab initio parametrization of density functional dispersion correction (DFT-D) for the 94 elements H-Pu. *J. Chem. Phys.* **132**, 154104 (2010).